

Transport in two-dimensional electron systems in
ZnO under the influence of microwave radiation

Transport in zweidimensionalen Elektronensystemen in
ZnO unter dem Einfluss von Mikrowellenstrahlung

Von der Fakultät Mathematik und Physik
der Universität Stuttgart zur Erlangung der Würde eines
Doktors der Naturwissenschaften (Dr. rer. nat.)
genehmigte Abhandlung

vorgelegt von
Daniel Kärcher
aus Stuttgart

Hauptberichter: Prof. Dr. Bernhard Keimer
Mitberichter: Prof. Dr. Peter Michler
Tag der mündlichen Prüfung: 15.01.2016

angefertigt am
Max-Planck-Institut für Festkörperforschung
Abteilung Keimer / von Klitzing
2016

Daniel Kärcher · Transport in two-dimensional electron systems in ZnO under the influence of microwave radiation · Dissertation · Max Planck Institute for Solid State Research · Stuttgart · Department Prof. Dr. Bernhard Keimer · Supervisor: Dr. Jurgen Smet · Co-Examiner: Prof. Dr. Peter Michler · Institut für Halbleiteroptik und Funktionelle Grenzflächen · University of Stuttgart · Chairperson: Prof. Dr. H. P. Büchler · Institut für Theoretische Physik III · University of Stuttgart · First edition: June 22nd, 2015 · Oral exam January 15th, 2016 · Final edition January 18th, 2016

Daniel Kärcher · Transport in zweidimensionalen Elektronensystemen in ZnO unter dem Einfluss von Mikrowellenstrahlung · Dissertation · Max-Planck-Institut für Festkörperforschung · Stuttgart · Abteilung Prof. Dr. Bernhard Keimer · Betreuer: Dr. Jurgen Smet · Mitberichter: Prof. Dr. Peter Michler · Institut für Halbleiteroptik und Funktionelle Grenzflächen · Universität Stuttgart · Prüfungsvorsitzender: Prof. Dr. H. P. Büchler · Institut für Theoretische Physik III · Universität Stuttgart · Erstabgabe: 22.06.2015 · Mündliche Prüfung 15.01.2016 · Finale Abgabe 18.01.2016

Contents

0.1	Introduction	6
I	Two-dimensional electron systems	9
1	Transport in two-dimensional electron gases	11
1.1	Classical transport: Electron mobility in the Drude model	12
1.2	Quantum transport	13
1.3	2DES in a magnetic field	14
1.4	Landau quantization	15
1.5	Shubnikov de-Haas oscillations	17
1.6	Quantum Hall Effect	19
2	ZnO heterostructures	21
2.1	Oxide film growth	22
2.2	Electric properties	24

3	Microwave-induced resistance oscillations (MIRO)	27
3.1	Theoretical approach	29
3.1.1	Displacement mechanism	30
3.1.2	Inelastic mechanism	32
3.1.3	Other theoretical approaches	34
3.2	Transport experiments	34
3.2.1	Frequency & phase dependence	35
3.2.2	Microwave power dependence	37
3.2.3	Temperature dependence	37
3.2.4	In-plane magnetic fields	38
3.2.5	Density, mobility & quantum lifetime dependence	38
3.2.6	Effective mass	39
3.2.7	Fractional MIRO	39
3.2.8	Zero resistance states (ZRS) and bistability	40
3.3	Photovoltage / Photocurrent measurements	40
3.4	Polarization experiments	43
3.4.1	Circular polarization	43
3.4.2	Linear polarization	45
II	Microwave-induced quantum oscillations in ZnO	47
4	Microwave-induced resistance oscillations	53
4.1	Frequency dependence	55

5	Photovoltage & Photocurrent measurements	59
5.1	Temperature dependence	63
5.2	Power dependence	67
6	Density dependence	71
7	Comparison of the quantum lifetime	73
7.1	τ_q from Shubnikov de-Haas oscillations	74
7.2	τ_q from MIRO	76
7.3	τ_q from MIPVO	81
7.4	Comparison	83
8	Summary	87
8.1	English	87
8.2	German	88
III	Appendix	91
9	Cyclotron resonance absorption	93
10	Electrical transport measurement setup	95
10.1	Avoiding ground loops	95
10.2	Signal cables	97
10.3	Common-mode rejection ratio (CMRR)	98
10.4	Asymmetric input resistances	99

Nomenclature

2DEG	two-dimensional electron gas
2DES	two-dimensional electron system
AC	alternating current
B	magnetic field
CM	common-mode
CMRR	common-mode rejection ratio
CRA	cyclotron resonance absorption
CRI	cyclotron resonance inactive
DC	direct current
δ_ω	MIRO detuning
e	elementary charge
ϵ_{ac}	ratio of microwave and cyclotron energy
E	electric field
E_F	Fermi energy
$E_H = \rho_H j$	Hall electric field
f_{MW}	microwave frequency
FET	field effect transistor
g	g-factor, Landée factor
$\hbar = h/2\pi$	(reduced) Planck constant
j	current density
k_B	Boltzmann constant
l_B	magnetic length
LL	Landau levels
m^*	electron effective mass
MIRO	microwave-induced resistance oscillations
μ	electron mobility
μ_B	Bohr magneton
μ_{ch}	chemical potential
n	charge carrier density
n_{LL}	Landau level degeneracy
P_{out}	microwave output power
ρ	resistivity
ρ_H	Hall resistivity
r_s	Wigner–Seitz radius

R	sample resistance
$R_L = R_{xx}$	longitudinal resistance
$R_H = R_{xy}$	Hall resistance
R_c	cyclotron radius
SdH	Shubnikov de-Haas (oscillation)
T	temperature
τ	transport (scattering) time
$\tau_{q,\text{SdH}}$	quantum lifetime from Shubnikov-de Haas oscillations
$\tau_{q,\text{MIRO}}$	quantum lifetime from MIRO
$\tau_{q,\text{MIPVO}}$	quantum lifetime from photovoltage oscillations
Θ	scattering angle
v_d	drift velocity
ν	filling factor
ω	microwave frequency
$\omega_c = eB/m^*$	cyclotron frequency
$\omega_H = 2R_c eE/\hbar$	Hall frequency
ZRS	zero-resistance states

0.1 Introduction

Reducing the dimensionality of physical systems is fundamentally interesting. It lets you think about the structure of our world and how it would look like if it did not consist of three dimensions (3D) in space. Today we are able to generate 2D, 1D and even 0D environments for electrons, by confining them to a limited number of spatial dimensions. As their degree of freedom to move shrinks, it has major implications for their interaction and kinetic behavior.

0D is the extreme case of confinement in all three dimensions. The electrons are not able to move anymore. Quantum physics tells us that the energy spectrum is quantized, allowing only for discrete energies to be occupied by the electron. This case is naturally realized for electrons, which are bound to atoms for example. Discovered back in the 19th century, spectral emission lines tell us about different energy states that electrons can occupy. Atomic physics is interested in how interactions between different electrons can shift these energy states.

In 1D systems, such as conductive polymers or quantum wires, electrons are free to move in one direction. The interaction between two electrons is still very high, because on a one-dimensional conductor electrons have to overlay each other to exchange positions. This is different compared to 2D or 3D systems. Here electrons are able to avoid each other in space. However in 2D systems there are only two possibilities of going around each other (left and right), compared to the manifold ways provided in 3D systems.

If magnetic fields are involved things get even more interesting. They cause the electron motion to become circular. In 2D systems the circular plane is intrinsically defined. If compared to 1D or 0D systems, where one cannot think about circular motion, and 3D systems, where small changes to the direction of the magnetic field are defining separate circular planes. The intermediate position of 2D systems in terms of freedom to move for the charge carriers makes them very interesting to study from a fundamental point of view.

Moreover, 2D systems are highly commercially relevant, since they are realized in field effect transistors (FET). Silicon technology, which is at the heart of every computer, tablet or smartphone uses FETs as the building blocks for electric circuitry and memory. Other material systems, such as for example

GaAs, InAs or the very recently discovered graphene offer the possibility of realizing 2D electron systems as well. Up to now they are not as commercially relevant as the well-established silicon technology, although their quality, in terms of undisturbed and therefore efficient electron movement, has overtaken silicon technology.

In fundamental science however there exists a run for cleaner and cleaner materials to study electron behavior in an utmost undisturbed way. During the last decade these efforts are approaching oxidic systems. They are of particular interest because very often the electron interactions are stronger compared to conventional semiconductor systems. Here ZnO heterostructures are at the spearhead in terms of undisturbed electron motion. They are providing today one of the cleanest conductive systems in the oxide world. In this thesis we want to investigate the electronic properties of ZnO heterostructures under the influence of microwave radiation and magnetic fields. This allows us to excite the electron system with microwave photon energies and probe the quantum nature of the electrons subject to magnetic fields. Experiments like the ones performed in this thesis allow for a better understanding of electron behavior in ZnO heterostructures. They tell us about interaction strengths and disorder and therefore describe how undisturbed this movement really is. This brings us to the main topic of this thesis, which is the discovery and characterization of microwave-induced resistance oscillations and related effects in ZnO heterostructures.

This thesis is divided into 3 parts:

Part I covers the fundamentals regarding electron transport in magnetic fields, the material system used in this work and about microwave-induced resistance oscillations. In chapter 1 we will deal with the basic properties of electron transport in two-dimensional electron systems. The influence of electric and magnetic fields is studied classically as well as quantum mechanically. Chapter 2 specifies this to ZnO heterostructures and covers the film growth and sample preparation. We will present how growth parameters influence the electronic properties. The fundamentals of microwave-induced resistance oscillations are covered in chapter 3.

These are the key ingredients to understand the experiments described in Part II. The finding of microwave-induced resistance oscillations (MIRO) is de-

scribed in chapter 4. Photocurrent and photovoltages provide an alternative experimental approach to the same physical effect. As it will turn out photovoltage signals are superior, compared to resistance signals, for studying temperature and power dependence as described in chapter 5. Chapter 6 provides an overview of various ZnO heterostructures with different electron densities. In chapter 7 both approaches together with Shubnikov de-Haas oscillations are used to study the quantum lifetime of electrons in ZnO heterostructures. A summary of the experimental findings and an outlook to future experiments is given in chapter 8.

The appendix part provides a description of experiments related to cyclotron resonance absorption in chapter 9. A practical guideline about electrical transport measurement setups is given in chapter 10.

Part I

Fundamentals: Two-dimensional electron systems

Chapter 1

Transport in two-dimensional electron gases

The following chapter introduces basic terms connected to electron transport, which are used in the thesis later on, such as the Drude model and related quantities like the electron mobility μ , scattering times τ and the quantum lifetime τ_q .

Afterwards we will cover the motion of electrons in a magnetic field. First we will provide a classical description. Subsequently Landau quantization of the density of states and its consequences for transport (Shubnikov de-Haas (SdH) oscillations and the quantum Hall effect (QHE)) will be addressed. For a broad introduction to the field of electric transport we would like to refer to [1, 2, 3].

As seen in the next chapter, electrons in ZnO heterostructures are confined due to band bending at the interface and therefore electron motion is quantized in the z-direction. For sufficiently low electron densities and temperatures only the lowest subband is filled, resulting in a truly 2 dimensional system with a

simplified energy dispersion in the framework of the effective mass approximation:

$$E = \frac{\hbar k_x^2 + \hbar k_y^2}{2m^*} + E_z. \quad (1.1)$$

Here k_x and k_y are the wave vectors in the two-dimensional xy-plane, m^* is the electron effective mass ($m_{\text{ZnO}}^* \approx 0.3m_e$) with m_e as the free electron mass and E_z as the zero energy offset of the first sub-band. The effective mass approximation simplifies the band structure near the bandgap of a semiconductor with a parabolic dispersion relation (like for free particles). Compared to experiments it turns out that this is a very good approximation for many material systems. Deviations from the effective mass approximation, which can occur for high carrier densities, i.e. high Fermi energies, are referred to as non-parabolicity effects.

1.1 Classical transport: Electron mobility in the Drude model

The concept of electrons in a crystal as free particles, which is called the Drude model [4], is still in use today. Electrons are accelerated by an electric field E , associated with a voltage drop ΔV across the sample. Due to different scattering processes the electron undergoes momentum changes and energy losses, which, if averaged out, lead to an overall drift velocity. Hereby the following assumptions are made: all electrons are equally contributing to the transport and scattering events are homogenous and isotropic. The resulting drift velocity v_d can be written (in a 1D form) as:

$$v_d = e\tau/m^*E \quad \text{with} \quad j = nev_d \quad \Rightarrow \quad j = ne^2\tau/m^*E. \quad (1.2)$$

Here the electron mobility $\mu = e\tau/m^*$ is a measure for the conductivity of electrons. Hereby the effective mass can be interpreted as a measure m^* of

how easily the electron can be accelerated and the scattering time τ of how much it is decelerated by scattering processes. It is interesting to mention that τ can be addressed by improving the crystal quality, while m^* is a parameter connected to the lattice structure itself.

Together with the electron density n the electron mobility μ directly relates the current density j to the applied voltage $V = E/d$, and therefore describes the electrical resistivity ρ .

$$\rho = E/j = E/(nev_d) = 1/(ne^2\tau m^*) = 1/(ne\mu) \quad (1.3)$$

Experimentally the resistivity $\rho = \sigma^{-1}$ is measured by imposing a current (usually with the help of a known resistor in series) and measuring the voltage drop across the sample. Rather than referring to the resistivity ρ we alternatively talk about the resistance $R = \rho * L/A$, since they are simply coupled by a geometric factor: here L is the sample length and A the sample cross-sectional area. The conductivity connects the current (density) through the sample and the applied electric field: $j = \sigma E$ and is measured by applying a voltage and measuring the current through the sample.

Although today we know about the limitations of the Drude model (e.g. not all electrons but only those near the Fermi energy E_F participate in transport), it is still used for its simple and intuitive character and the electron mobility is one of the key indicators of sample quality.

1.2 Quantum transport

In literature quantum transport is separated to conventional or classical transport, if the wavelike nature of electrons plays a role. This introduces the phase factor as an additional parameter to describe the electrons. While in classical transport scattering events lead to a resistivity in quantum transport also the phase of the electron wave function is affected by scattering processes.

Therefore one can divide scattering processes into small angle (forward) and large angle (backward) scattering events. Only large angle scattering events result in electrical resistance and are connected to, what has been defined as,

the electron mobility μ and the transport time τ as defined in the previous section. The phase factor is randomized during a scattering process. Small angle scattering events do not change the momentum of the electrons but still randomize the phase of the wave function. Small angle scattering processes have no effect on classical quantities such as resistance or electron mobility. The characteristic time between two scattering events that randomize the phase is called the quantum lifetime τ_q . Large angle scattering also randomizes the phase and $\tau > \tau_q$.

There is a continuous transition from large angle to small angle scattering, which makes this separation of scattering events into two distinct groups (large angle and small angle scattering) somewhat artificial. Nevertheless it helps characterizing the electronic system and provides insight into the scattering mechanism of electrical systems.

The exact definitions for τ and τ_q are as follows:

$$\tau^{-1} = \int f(\Theta)(1 - \cos \Theta)d\Theta \quad (1.4)$$

$$\tau_q^{-1} = \int f(\Theta)d\Theta. \quad (1.5)$$

Here Θ is the scattering angle, $f(\Theta)$ is the scattering probability for the respective angle Θ . One can see that while τ mainly covers large angle scattering events, τ_q accounts for all of them. The ratio τ/τ_q can be used to identify dominate scattering mechanisms. Generally the sharper the scattering potential is the higher the probability of large angle scattering events.

For further explanations we want to refer to literature [1, 5].

1.3 2DES in a magnetic field

Classically an external homogenous magnetic field, oriented perpendicular to the two-dimensional electron system, forces the electrons to a circular motion with a radius of R_c (cyclotron radius) and an angular frequency of ω_c (cyclotron

frequency).¹ This force is called the Lorentz force.

$$R_c = l_B^2 k_F, \quad \omega_c = eB/m^*. \quad (1.6)$$

Here $l_B^2 = \hbar/eB$ sets a characteristic area or length scale in the system (referred to as magnetic length). If a current is passed through a sample with an applied perpendicular field a Hall voltage builds up to compensate for the Lorentz force. This is described by the Hall resistivity ρ_H (while classically the longitudinal resistivity is not affected by the magnetic field):

$$\rho_H = B/(ne) \quad (1.7)$$

The conductivity and resistivity become tensors, which complicates their relation to a tensor inversion. Details on this can be found in almost any solid state physics textbook, e.g. [2, 1, 3]. Hall measurements are used to determine the charge carrier density n and their charge (electron or hole systems).

1.4 Landau quantization

Quantum mechanically the influence of a magnetic field is considered as a correction to the momentum operator represented by a vector potential.² The magnetic field quantizes the electron energy spectrum into discrete energy levels, if $\hbar\omega_c \gg k_B T$ and $\mu \cdot B \geq 1$. They are referred to as Landau levels (LL) and are equidistant in energy E_n (for parabolic energy dispersions) and equally degenerate n_{LL} .

$$E_n = \hbar\omega_c(n + 1/2) \quad n_{LL} = 2eB/h \quad (1.8)$$

The factor 2 in the Landau level degeneracy comes from the spin degeneracy

¹For the sake of simplicity we consider systems with a circular Fermi surface

²There is no unique definition for the vector potential to describe a magnetic field perpendicular to the 2DEG. The remaining freedom is mathematically described by a gauge factor. Here usually the so called Landau gauge offers the simplest solution.

and applies for GaAs and ZnO systems. (It is larger in systems with higher intrinsic degeneracy).

The condition $\omega_c\tau > 1$, which means that electrons fulfill complete circles, without any scattering event in between (which would randomize their momentum), leads to self-interference of electrons. The energy spectrum is then quantized into discrete values E_n , which also correspond to discrete values for the cyclotron radii R_c . The Hall resistivity ρ_H is then larger than the longitudinal resistivity ρ_L .

It is important to mention that, while the LL energy is dependent on material properties (namely the electron effective mass m^* , which enters the cyclotron frequency ω_c) the LL degeneracy is universal. The LL degeneracy is only dependent on the magnetic field, but not on the sample details like disorder, electronic band structure, etc.

For higher magnetic fields the spin degeneracy can be lifted due to the Zeeman energy term:

$$E_z = g\mu_B B \qquad \mu_B = e\hbar/2m \qquad (1.9)$$

with μ_B as the Bohr magneton and g as the Landé factor.

The filling factor ν states how many LL are occupied:

$$\nu = n/n_{LL} \qquad (1.10)$$

LL were introduced as energetically degenerate states, which only holds for systems in the absence of scattering. The finite coherence time of electrons causes a LL broadening, described by the quantum life τ_q . Hereby the uncertainty principle leads to an energy broadening of

$$\delta E = \hbar/\tau_q \qquad (1.11)$$

The next section deals with the Shubnikov de-Haas effect which is a manifestation of LL quantization in electric transport measurements.

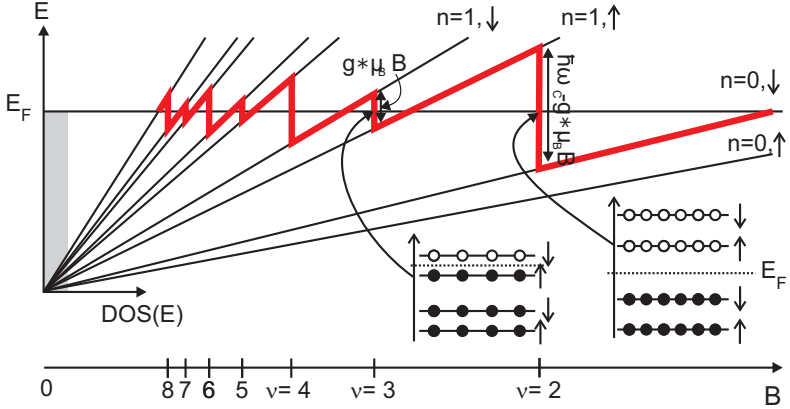


Figure 1.1: Evolution of the chemical potential μ_{ch} (red) in the context of spin-split Landau quantization as a function of magnetic field. The increasing LL energy and degeneracy leads to jumps in the chemical potential and an overall sawtooth-like behavior (adopted from [6]).

1.5 Shubnikov de-Haas oscillations

The Shubnikov de-Haas (SdH) effect is a purely quantum mechanical effect, defined as an oscillatory change in resistivity. Therefore it is a prominent example of solid state quantum physics as oscillations in the resistivity show the quantum nature of the microscopic electrons.

If a magnetic field is ramped up in experiment, while keeping the carrier density in the 2DEG constant, the energy of each LL raises linearly with B with an increase of the LL degeneracy at the same time. The chemical potential is pinned to the uppermost filled LL until the degeneracy of the lower lying LLs is high enough to accommodate all charge carriers. At this point the chemical potential μ_{ch} jumps and is again pinned to the next lower LL (refer to Figure 1.1). For a fixed charge carrier density n the density of states (DOS) at the Fermi energy E_F and the resistivity are oscillating at a $1/B$ periodicity (please refer to Figures 2.3 and 4.1).

Every time the chemical potential jumps, the electronic system undergoes a metal-insulator transition with zero conductivity. Due to the tensor relation of conductivity and resistivity in a magnetic field, the resistivity is zero at the same time as the conductivity is.

As the SdH oscillations are a self-interference effect of the electrons, their phase coherence is important: SdH oscillation amplitudes are sensitive to all scattering processes (and therefore to the quantum lifetime τ_q). They can be mathematically described as follows [7, 8]:

$$\frac{\Delta R}{4R_0} = \frac{A_T}{\sinh(A_T)} 4 \exp(-\pi / \omega_c \tau_q), \quad \text{with} \quad A_T = 2\pi^2 k_B T / \hbar \omega_c \quad (1.12)$$

Here A_T is the thermal smearing coefficient, relating the thermal energy $k_B T$ to the cyclotron energy $\hbar \omega_c$.

The next section describes how the quantum lifetime can be extracted from the dampening of SdH oscillations amplitude

Determination of the quantum lifetime

The quantum lifetime τ_q of the electrons enters the amplitude dampening of SdH oscillations. The exponential term $\exp(-\pi / \omega_c \tau_q)$ in formula 1.12, also called Dingle factor, is dependent on the quantum lifetime τ_q to the cyclotron frequency ω_c .

To extract the quantum lifetime τ_q the SdH extrema are plotted in a so-called Dingle plot in which $\ln\left(\frac{\Delta R}{4R_0} \cdot \frac{\sinh(A_T)}{A_T}\right)$ is plotted against $1/B$. According to formula 1.12 this brings all extrema on a linear projection with a slope of $(-\pi m^* / e \tau_q)$. It therefore makes the quantum lifetime τ_q accessible, if the electron effective mass m^* is known.

Dingle plot analyses can be done in a magnetic field range limited by the onset of SdH oscillation and the spin-splitting. To separate SdH oscillations that belong to different spin subsystems one needs to model the spin-splitting appropriately. Here it is still under debate which shape of LL broadening should

be chosen: some publications support Gaussian shape [9, 10, 11] while others come up with Lorentzian shape [12, 13].

1.6 Quantum Hall Effect

The quantum Hall effect (QHE), discovered by Klaus v. Klitzing in 1980 [14, 15] was honored by the Nobel Prize in 1985. It is closely related to the physics of Landau quantization and should therefore be mentioned at this point here for the sake of completeness. For a short and comprehensive introduction please refer to [6].

For completely separated LL ($\omega_c\tau_q > 1$) the sample edges become important [16] for electron transport and current is redistributed in a way that at the same time backscattering is forbidden [17] and therefore the longitudinal resistance R_L is zero [18, 19]. At the same time the Hall resistance R_H is quantized to fractions of the fundamental resistance, defined by the Planck constant h and the elementary charge e .

$$R_H = \frac{h}{ie^2} \quad i = 1, 2, 3, \dots \quad R_L = 0 \quad (1.13)$$

The quantized resistance values are independent from sample parameters, both macroscopically (size, geometry, etc) and microscopically (disorder, doping, imperfections, etc).

The integer QHE can be treated without taking interactions between electrons into account (so called single particle picture). However, electron–electron interaction leads to new and very exciting physics, such as the fractional quantum Hall effect [20, 21] and its more exotic states like $5/2$ [22], triggering a major interest in quantum computing by exploiting novel quasiparticles [23].

Chapter 2

ZnO heterostructures

This thesis covers ZnO heterostructures and the two-dimensional (2D) electron systems they host. There is a variety of different realizations of 2D systems, that follow different approaches on how the electrons are confined in one dimension.

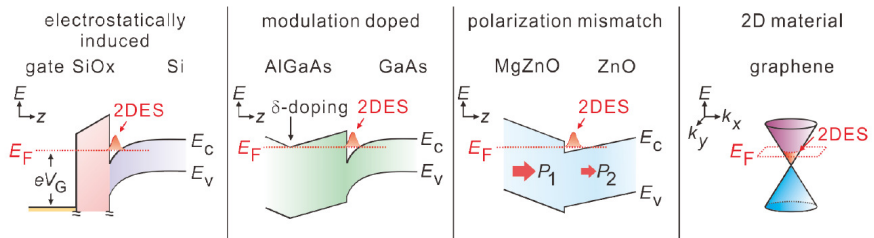


Figure 2.1: Overview on the different realizations of two-dimensional electron systems (2DES). (taken from [24])

Figure 2.1 shows four different configurations for the realization of two-dimensional electron systems (2DES). The first three (Si/SiO₂, GaAs/AlGaAs, ZnO/MgZnO) have in common, that a confinement potential is formed at

the interface of two different material systems. The energetic minimum in z -direction forces the electrons to stay in the 2D plane. Graphene inherently hosts a 2DES, since the material itself consists of a 2D structure.

Different growth techniques are used to fabricate these heterostructures, for instance chemical vapor deposition (CVD), physical vapor deposition (PLD), and molecular beam epitaxy (MBE). The samples used in this thesis are grown in a special MBE chamber using ozone as a very pure source of oxygen. Therefore one talks about oxide molecular beam epitaxy (OMBE). Apart stands the exfoliation of graphene, which, in contrast to the mentioned bottom-up techniques, is a top-down approach: a graphite crystal consisting of graphene sheets is cleaved and thinned down using a scotch tape.

2.1 Oxide film growth

The goal of the growth of high quality oxide films is the reduction of the concentration of crystal defects and dislocations as well as impurities to a minimum level. The quality can be validated by various physical characterization tools, like optical microscopy, atomic force microscopy or x-ray diffraction. As it turns out for very clean material systems, such as GaAs or ZnO heterostructures, these physical characterization tools are already at the limit and cannot differentiate between clean and ultra-clean samples. Nowadays it is possible to fabricate a variety of semiconductor materials with a purity of 99.999999%. In the case of 2-dimensional electron systems (2DES), electrical characterization has proven to be the most sensitive tool to judge crystal cleanliness [25]. The basics of electrical transport in 2DES is covered in chapter 1.

For most semiconductor growth the formation of oxygen bonds leads to strong disorder acting as scattering centers for the electrons. Removing any oxygen content in the growing chamber leads to an enormous increase in effort (turbo-pumps, cryo-pumps, ion sublimation pumps, ...). Although good vacuum quality also helps growing ZnO heterostructures, the need of strictly avoiding oxygen contamination is not given in oxide film growth.

Efforts in various directions have led to great success in the field of oxide film growth, as covered by a recent review article by Hwang, Iwasa, Kawasaki,

Keimer, Nagaosa and Tokura [26].

ZnO heterostructures used throughout this thesis are grown by oxide molecular beam epitaxy (OMBE) and the use of pure liquefied ozone. The sample preparation was carried out by J. Falson¹. He used high-quality 10 mm x 10 mm x 0.35 mm ZnO substrates with Zn-polarity grown by the hydrothermal method by Tokyo Denpa as a starting material. The substrates were etched in hydrochloric acid to remove residual dirt from the substrate polishing and cutting. The acid also removes a thin layer of ZnO, providing a clean surface [27]. After the substrate has been loaded to the OMBE machine a high temperature annealing under high vacuum further improves the surface quality. Very high vacuum quality (10^{-8} Pa) can be reached by cooling the growth chamber with liquid nitrogen. Residual gas molecules, that are not pumped away by the turbo pump, are adsorbed by the cold walls of the chamber, acting as a so called cryo-pump. This very low pressure gives a mean free path for gas molecules of 10^6 m.

The use of liquified distilled ozone as an oxygen source during growth turns out to be a key advance. It provides a very clean way of oxidizing Zn or Mg. This advantage can be addressed to the chemical properties of ozone, compared to oxygen plasma (which is commonly used in OMBEs). Because of the higher reaction rates of ozone the growth temperature can be reduced by more than 100° C, leading to fewer dislocations and more homogeneous crystal quality. As an effect, the electron mobilities in ZnO heterostructures have increased from $150,000 \text{ cm}^2(\text{Vs})^{-1}$ to above $700,000 \text{ cm}^2(\text{Vs})^{-1}$ within the last years.

During OMBE a ZnO buffer layer is grown on top of the ZnO substrate followed by a MgZnO capping layer. The actual 2DEG forms in the ZnO buffer layer, next to the heterointerface. Starting from a capping layer thickness of 30 nm, a 2DEG is induced in the ZnO buffer layer. There is a tendency towards higher electron mobilities μ with increasing capping layer thickness. Samples were grown up to a capping layer thickness of 1000 nm.

¹Department of Applied Physics and Quantum-Phase Electronics Center (QPEC), University of Tokyo, Tokyo 113-8656, Japan and RIKEN Center for Emergent Matter Science (CEMS), Wako 351-0198, Japan

2.2 Electric properties

The ZnO heterostructure samples are consisting of two materials: ZnO and $\text{Mg}_x\text{Zn}_{x-1}\text{O}$. As pointed out in the previous section $\text{Mg}_x\text{Zn}_{x-1}\text{O}$ is grown on top of ZnO during the growth process.

ZnO itself is an interesting material with various applications [28]. It forms a Wurtzite crystal structure with a bandgap of 3.37 eV with an intrinsic polarization field. $\text{Mg}_x\text{Zn}_{x-1}\text{O}$ has a different magnitude of the polarization field, depending on the stoichiometry. It is exactly this polarization field mismatch, which is exploited in ZnO/MgZnO heterostructures to form a two-dimensional electron gas (2DEG) at the interface². Due to charge accumulation of the interface and the associated electrostatic forces a triangular shaped potential well is formed by the ZnO conduction band in conjunction with the band-offset at the interface.

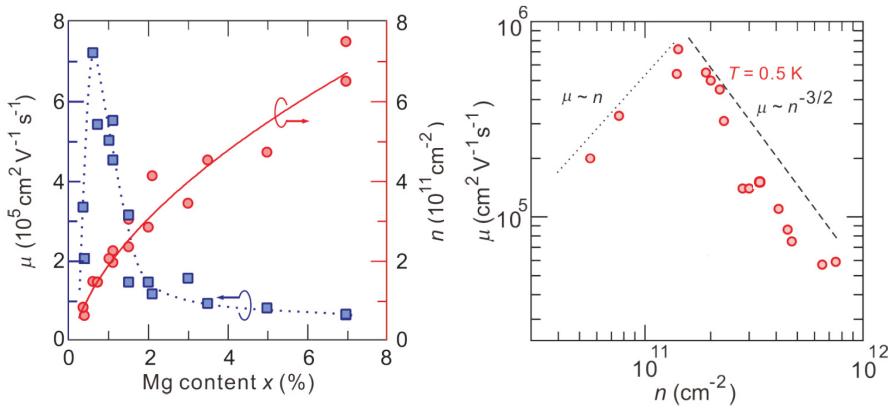


Figure 2.2: Left: Electron mobility μ and electron density n as a function of the growth parameter magnesium (Mg) content. Right: Same data plotted as electron mobility μ vs. electron density n . (adopted from [24])

²The formation of a 2DEG in AlGaIn/GaN heterostructures is analogous and also in a Wurtzite crystal structure

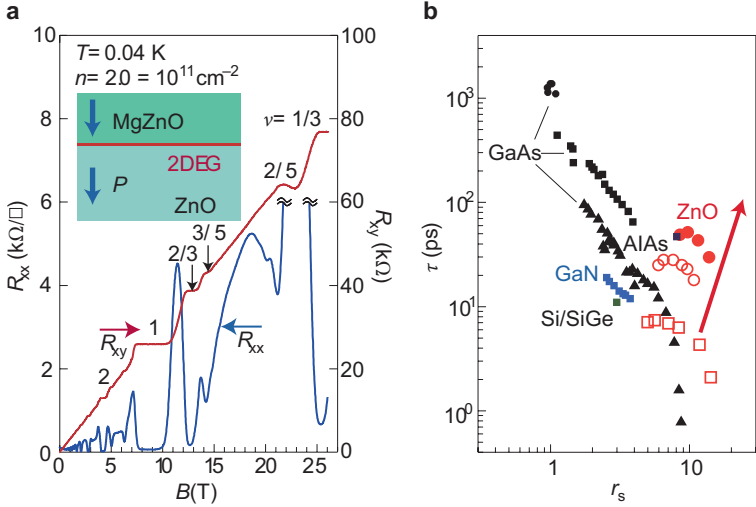


Figure 2.3: (a) Longitudinal resistance R_{xx} and Hall resistance R_{xy} of a 2DEG formed at a ZnO/MgZnO interface. The longitudinal resistance R_{xx} shows Shubnikov de-Haas (SdH) oscillations and the integer and fractional quantum Hall effects. The Hall resistance R_{xy} shows plateaus of the integer and fractional quantum Hall effects (QHE) (b) Comparison of transport time τ and Wigner Seitz radius r_s for various semiconductor systems. The red arrow indicates a part of the parameter space to which ZnO is moving and which is hard to access in semiconductor systems. (taken from [26])

Using a set of samples with varying magnesium content, it can be shown that both, the electron density n and the electron mobility μ strongly depend on the Mg content x . These results from [29, 24] are depicted in Figure 2.2. An optimum magnesium content of 1% is found to maximize the electron mobility. Values up to $700,000 \text{ cm}^2(\text{Vs})^{-1}$ can be reached.

Compared to conventional semiconductors, electrons in ZnO have different properties. Due to the oxidic character of the material a high effective mass $m_{\text{ZnO}}^* = 0.29 m_e$ [28] lowers the kinetic energy. Therefore the Coulomb interaction becomes more important. The ratio of Coulomb energy E_C to Fermi

energy E_F is defined as the Wigner–Seitz radius r_s :

$$r_s = \frac{E_C}{E_F} = \frac{e^2 m^*}{2\pi\epsilon\hbar^2\sqrt{\pi n}} \quad (2.1)$$

Achieving high quality 2DEGs in oxides, such as the ZnO heterostructures used in this thesis opens up the exploration of new parameter spaces. As a manifestation of this, Figure 2.3(a) shows the fractional quantum Hall effect in ZnO heterostructures and (b) an overview of the scattering time τ and the Wigner–Seitz radius r_s for different material systems.

Moreover ZnO has a high g-factor $g_{\text{ZnO}} = 3.86$, compared to GaAs ($g_{\text{GaAs}} = -0.44$ [24]). Hence the cyclotron energy E_c and Zeeman energy E_z are comparable in ZnO and the ratio is a factor of 40 bigger than in GaAs.

Chapter 3

Microwave-induced resistance oscillations (MIRO)

This thesis deals with microwave-induced resistance oscillations (MIRO) in ZnO heterostructures. The necessary background information to understand these effects is provided in the following chapter. It is not meant as a comprehensive list of experiments, but rather tries to summarize the most important experimental findings. It also introduces the two most commonly used theories to describe the effect.

Figure 3.1 displays magneto-transport data recorded in the absence (top panel) and presence (bottom panel) of microwave radiation. In the top panel only Shubnikov de-Haas oscillations are observed. In the bottom panel a new type of oscillation shows up. This new type of oscillation is called microwave-induced resistance oscillation (MIRO) and was discovered in 2001 [30, 31]. The periodicity of the oscillations is governed by the ratio of photon and cyclotron energy, $\epsilon_{ac} = \omega / \omega_c$. Integer values of ϵ_{ac} correspond to oscillation nodes and the resistance is reduced for ϵ larger than the integer and enhanced for ϵ_{ac}

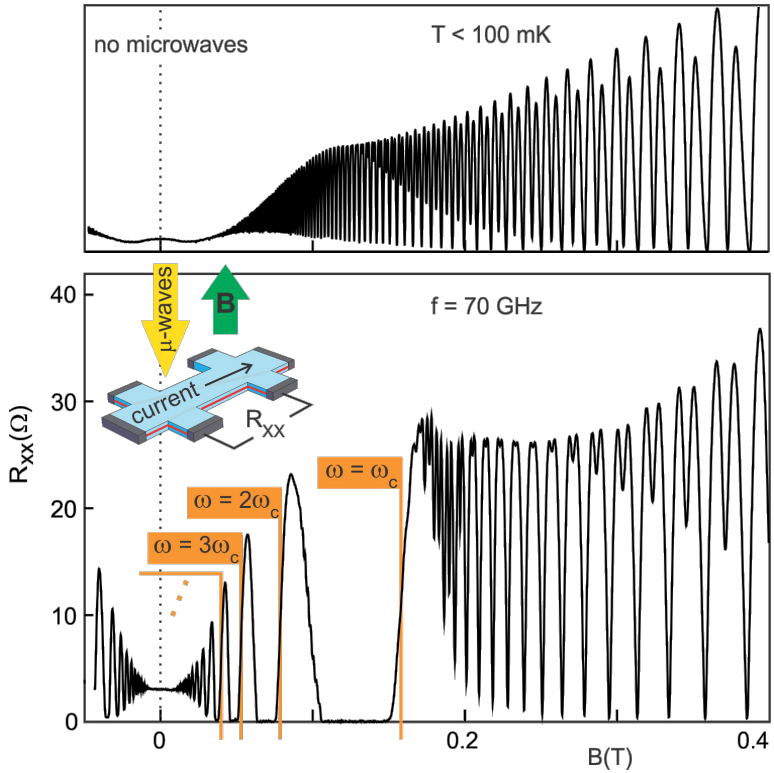


Figure 3.1: Shubnikov de-Haas oscillations in GaAs heterostructure with (bottom) and without (top) microwave radiation (taken from [6]).

smaller than the integer value. If MIRO are pronounced (as in the experiment in Figure 3.1) the resistance reduction is so strong that zero-resistance states (ZRS) are observed. These states were discovered shortly after MIRO in 2002 [32] and raised a lot of attention. Because zero resistance has been associated with such fundamental phenomena as the quantum Hall effect and superconductivity, the observation of microwave induced zero resistance states served as a strong driving force for research in this field [33, 34] .

For strongly overlapping Landau levels the enhancement and reduction of the resistance, around integer ϵ_{ac} , results in a $1/B$ periodic oscillation, resembling Shubnikov de-Haas oscillations, but the Hall resistance (not shown in Figure 3.1) is unaffected by the microwave radiation and does not display slope changes or plateaus.

Prior to 2014 MIRO have only been seen on GaAs/AlGaAs systems and in some experiments for electrons on the surface of liquid helium [35, 36]. The work presented in this PhD thesis and work by Zudov et al. [37] extended the MIRO family to ZnO and SiGe heterostructures.

3.1 Theoretical approach

In the following sections two distinct theoretical approaches to explain MIRO will be presented. They are called displacement and inelastic mechanism and represent the two most cited theories. At very low temperatures (<1 K) the inelastic mechanism is believed to dominate, while the displacement mechanism mainly contributes at elevated temperatures (1–10 K) in the presence of short-range scatterers. The inelastic mechanism has an additional temperature dependence term ($\propto T^{-2}$), compared to the displacement mechanism and therefore both mechanisms can be distinguished in experiment. We refer to the experimental part on temperature dependent MIRO in ZnO for a more detailed discussion (section 5.1). Both mechanisms are heavily depending on the type of disorder (smooth disorder, sharp disorder) in the system. Inelastic and displacement mechanism can coexist at intermediate temperatures resulting in two distinct scattering channels to relax the microwave excited electrons.

Preface on optical selection rules for LL transitions For microwave excitation of a 2DEG with $\epsilon_{ac} = 1$, one would expect a change in the transport behavior due to electronic excitations into the first unoccupied Landau level or even into higher ones via a ladder process. But if the photon energy corresponds to multiples of ϵ_{ac} , excitations are forbidden, because the transition matrix element for electrons equals 0 if the orbital index of the initial and final LL differs by more than one. (this is only true for clean systems without short range scatterers):

$$\langle j | Ex | j' \rangle = 0 \quad \text{for} \quad j' \neq j \pm 1 \quad (3.1)$$

The excitation with $\epsilon_{ac} = 1$ is known as the cyclotron resonance absorption (CRA) and has been widely used to determine the cyclotron mass of an electronic system.

3.1.1 Displacement mechanism (photon assisted impurity scattering)

Long before the experimental discovery of MIRO, Ryzhii et al. theoretically investigated the influence of microwaves on the transport behavior. They addressed photoconductivity signals and the possibility of obtaining negative resistance that might occur [38, 39].

Central to their model is photon assisted impurity scattering. Photon absorption is possible at any value of ϵ_{ac} and irrespective of the difference in the orbital index of the involved LLs because the electron scatters off an impurity and therefore equation 3.1 is no longer valid.

If a current runs through the sample, which is deflected by the magnetic field, a Hall voltage builds up, which is oriented perpendicular to the current. This Hall potential drop across the sample tilts the Landau levels (LL). When ϵ_{ac} is not an integer value, the excitation of the electron into a higher LL must be accompanied by a lateral displacement in order to fulfill energy conservation. This displacement process is schematically illustrated in Figure 3.2.

LL are strongly overlapping for small magnetic fields and are therefore taken

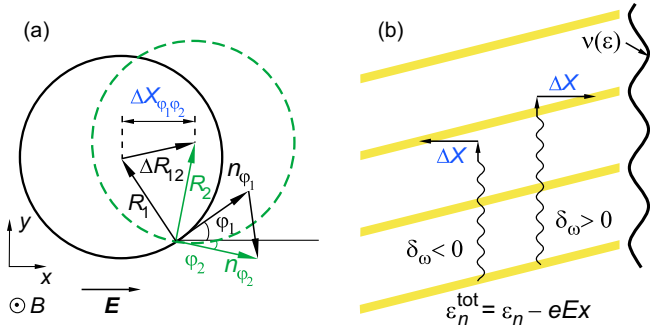


Figure 3.2: Schematic of the MIRO displacement mechanism. (a) Shift of guiding center of cyclotron orbit and momentum transfer. (b) Energy diagram of photo excitation and spatial displacement (taken from [40]).

into account as an oscillating density of states $\nu(\epsilon)$. The actual MIRO excitation is theoretically treated as a one step scattering channel, but can be described in three parts:

- A microwave photon is absorbed by the 2DES and one electron is excited (microwave photon absorption goes along with an elastic scattering process).
- The electron is scattered from an impurity (short range scattering disorder) and spatially displaced ΔX in a way that the electron ends up in a higher Landau level.
- The displacement in real space goes along with a displacement in momentum space, which is always perpendicular to the first one. This can be easily seen from Figure 3.2.

If one looks at the energy diagram in Figure 3.2, one can see that for microwave photon energies, which are slightly lower than a LL transition energy ($\delta_\omega < 0$), the displacement happens downhill in energy, leading to an increase in the longitudinal resistance and vice versa for photon energies slightly higher

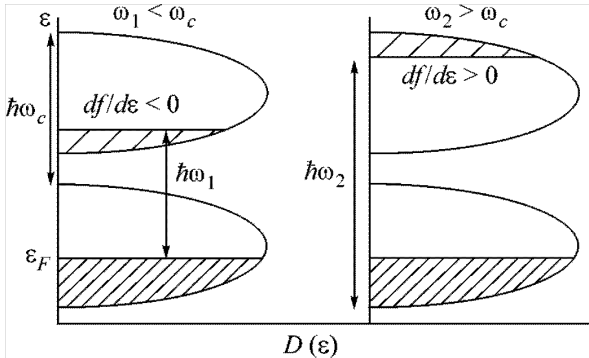


Figure 3.3: Basic schematic of the MIRO non-equilibrium distribution function (NEDF) mechanism (taken from [45]).

than a LL transition energy ($\delta_\omega > 0$). A downhill displacement implies an increase of the resistivity, whereas an uphill displacement causes the resistivity to drop.

More detailed quantitative explanations of the displacement mechanism can be found in [41, 42, 43, 44].

3.1.2 Inelastic mechanism (non-equilibrium distribution function)

The idea, that the incident microwave radiation induces a non-equilibrium energy distribution of the electrons was first discussed by S. Dorozhkin [45] and further developed by Dmitriev et al. [46, 47].

In the displacement model it is implicitly assumed, that excited electrons relax back fast enough in comparison with the excitation rate, so that there is no significant steady-state redistribution of electrons across the density of states. At lower temperatures however this assumption may no longer be valid and the microwaves may cause a population inversion:

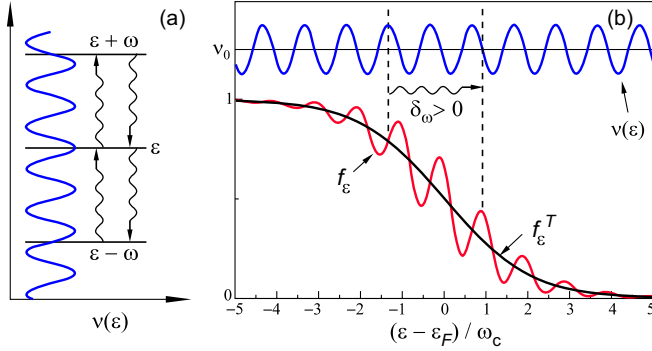


Figure 3.4: (a) Emission and absorption of microwave photons in the context of an oscillating density of states $\nu(\epsilon)$ (b)Non-equilibrium distribution function (NEDF) $f(\epsilon)$, normal Fermi distribution function $f_T(\epsilon)$ and LL modulated density of states $\nu(\epsilon)$ (taken from [40]).

1. Depending on the detuning of microwave and cyclotron energy δ_ω the constant irradiation (microwave absorption and emission) of the two-dimensional electron system leads to a redistribution of the electrons in the overlapping Landau levels (as depicted in Figure 3.3 and 3.4(a)). Especially the derivative of the distribution function with respect to energy at the upper end is influenced by the detuning. The consequence is an oscillating Fermi distribution function, which can be calculated as a stationary solution of the kinetic equation. This also involves inelastic relaxation by electron-electron interaction and energy diffusion caused by impurity scattering.
2. Combining the oscillating Fermi distribution function (caused by microwave radiation) with the oscillating density of states (caused by LL quantization) it can be shown by calculation that the oscillatory behavior survives energy averaging and leads to a resistance oscillation as δ_ω or (closer to the experiment) B is changed. This is illustrated in Figure 3.4.

We refer to a recent review by Dmitriev et al. for a quantitative description of this inelastic model and how it is related to the displacement mechanism [40].

3.1.3 Other theoretical approaches

Even though by now a consensus has been reached among the larger part of the theory community that the above theories account for the key experimental observations, a selection of other theories besides displacement and inelastic mechanism are listed here for the sake of completeness:

- Quasi-classical memory effects [48]
- Quadrupole and photovoltaic mechanisms [49]
- Ponderomotive forces near contacts [50]
- Photon assisted phonon scattering (acoustic mechanism) [51, 52, 53]
- Non-parabolicity effects for linear microwave polarization [54]
- Photon affected dressed density of states [55, 56]
- Perturbative treatment of semiclassical scattering [57]
- Edge channel transport stabilization [58]
- Synchronization [59]

3.2 Transport experiments

Transport experiments have been mainly carried out in the Hall bar geometry, although MIRO does not rely on a specific geometry. Experiments also show MIRO in the van der Pauw and Corbino geometry. The latter gives access to the conductivity, rather than the resistivity of the sample. The results are as expected from an inversion of the resistivity tensor [60].

The following sections give an overview on the experiments done so far. If not stated otherwise all experiments are done on GaAs/AlGaAs heterostructures, in the Hall bar configuration. The MIRO oscillations can often be described by the following empirical formula for the microwave induced resistivity correction:

$$\delta\rho_\omega = -A_\omega \epsilon_{ac} \lambda^2 \sin 2\pi \epsilon_{ac}. \quad (3.2)$$

Here $\epsilon_{ac} = \omega/\omega_c$, with $\omega = 2\pi f$ is the microwave frequency and $\omega_c = eB_\perp/m^*$ is the cyclotron frequency (m^* is the electron effective mass), $\lambda = \exp(-\epsilon_{ac}/2\epsilon_0)$ is the Dingle factor and $\epsilon_0 = f\tau_q$, τ_q being the quantum lifetime. A_ω is an amplitude prefactor, capturing all additional dependencies (for instance power and temperature dependence).

3.2.1 Frequency & phase dependence

MIRO are observed most pronounced within a frequency window of 30 and 170 GHz (minimum reported frequency: 3 GHz [61], maximum 1.5 THz [62]). All publications agree that MIRO features move linearly on a magnetic field axes, while changing the frequency. MIRO shift to lower magnetic fields for lower frequencies. They are exponentially suppressed by the Dingle factor $\lambda = \exp(-\pi/\omega_c\tau_q)$. The high frequency limit is governed by a $1/\omega^4$ dependency [60, 63].

The onset of MIRO on the magnetic field axis does not depend on frequency but on the quantum lifetime τ_q . This can be seen from [32, 61]. The quantum lifetime can be deduced from the onset of the MIRO oscillations, which occur roughly at $\omega_c\tau_q = 1$, i.e. the electron can complete a full cyclotron orbit without scattering.

The first and second MIRO extrema ($\epsilon_{ac} \approx 1, 2$) show different phases for minima and maxima which can have two reasons. First, larger magnetic fields lead to a more pronounced separation of LL and therefore cause changes to the harmonic resistance oscillation. Second, screening effects mainly come into play for the first and second MIRO extrema and change the shape of minima and maxima. Therefore very often the first two or three MIRO extrema are excluded in a quantitative analysis [40]. Please refer to [64] for a detailed consideration of the period and the phase of MIRO.

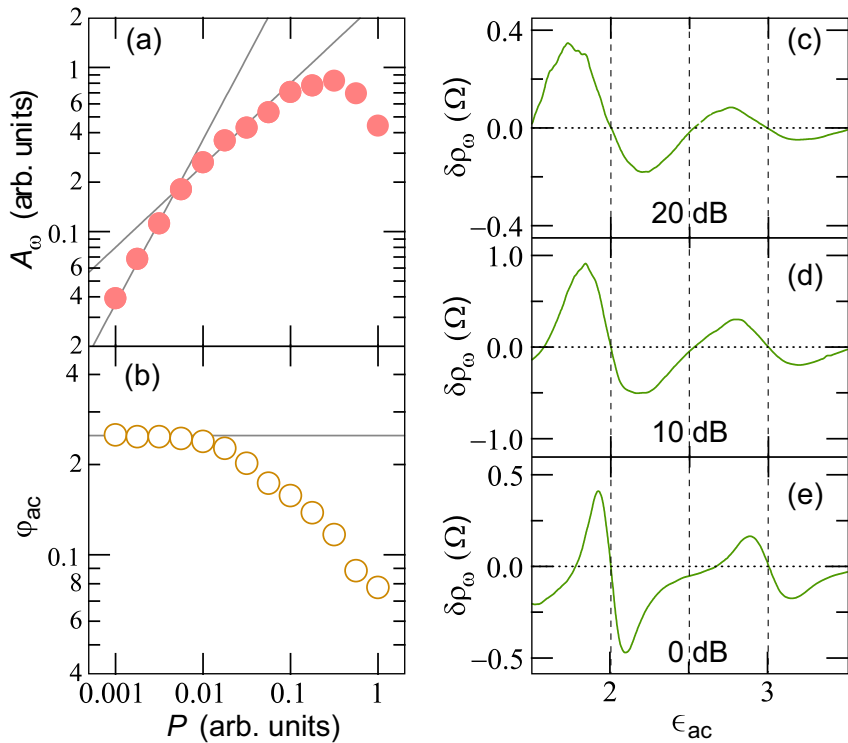


Figure 3.5: Influence of the microwave power P on the MIRO amplitude (a) and phase (b) as well as the shape of the oscillations (c-e). (taken from [40])

3.2.2 Microwave power dependence

The dependence of the MIRO amplitude on the microwave power is contained in the prefactor A_ω in equation 3.2. Some publications report a linear dependence [65, 66], while others report a sublinear dependence [31, 61]. This contradiction can be resolved by considering that the microwave radiation may heat up the system, so that with an increase of microwave power MIRO are also changed as a result of the modified electron temperature. The rise in temperature with microwave power is specific to the equipment as it depends on the cooling power of the cryogenic system.

A publication by Hatke et al. [67] reports a crossover from a P to $P^{1/2}$ dependence (as can be seen in Figure 3.5(a)). If the absorbed microwave power is larger than the cooling power, the MIRO amplitude decreases as a result of the heating of the electron system (see MIRO temperature dependence). The crossover from linear to square-root power dependence is expected for the inelastic mechanism as well as for multi phonon processes within the framework of the displacement mechanism [40]. Also the phase and shape of the oscillations are affected as seen in Figure 3.5(b,c-e) for very high microwave power.

Experimentally it is very difficult to measure the microwave power that is incident on the sample in transport experiments. When measured with the use of a microwave divider somewhere along the transmission line one has to be careful interpreting these values, because of the formation of standing waves which cause a very inhomogeneous spatial power distribution inside the sample rod, varying also rapidly with frequency.

3.2.3 Temperature dependence

MIRO can be observed best in a temperature regime of 0.5–1 K. They are strongly suppressed for higher temperatures.

The temperature dependence in the regime of low magnetic fields and low microwave powers stems from two factors: First temperature gives a quadratic correction to the quantum lifetime τ_q , which enters the Dingle factor λ in equation 3.2:

$$1/\tau_q^*(T) = 1/\tau_q + \alpha T^2 \quad (3.3)$$

Theory attributes this temperature dependence to LL broadening introduced by electron–electron interaction [68, 40]. Second, for the inelastic mechanism also the amplitude prefactor A_ω is expected to scale with $1/T^2$, whereas for the displacement mechanism no temperature dependence for A_ω is predicted. A $1/T^2$ dependence has indeed been observed in experiment [69]. An exception is data reported by Hatke et al. in [70], where this $1/T^2$ dependence could not be reproduced. Depending on the type of disorder, different mechanisms (inelastic mechanism, displacement mechanism) may dominate and hence samples may exhibit different temperature dependencies.

3.2.4 In-plane magnetic fields

The influence of an in-plane magnetic field on MIRO remains controversial: so far 3 reports have been published. Two of them show a strong suppression of MIRO when applying an in-plane magnetic field on the order of 1 T [71, 72]. Bogan et al. interpret this suppression of MIRO as the result of a correction to the quantum lifetime τ_q (entering the Dingle factor λ), caused by the in-plane magnetic field ($\propto B_{\parallel}^2$) (refer to equation 3.2). In contrast, Mani et al. assert that in-plane magnetic fields up to 1.2 T leave the MIRO oscillations unchanged [73].

3.2.5 Density, mobility & quantum lifetime dependence

MIRO were discovered in high mobility GaAs samples. Strong MIRO are observed almost exclusively in samples with $\mu > 10 \cdot 10^6 \text{ cm}^2/\text{Vs}$ [40], except for work published by Bykov et al. who used a sample with an electron mobility of only $\mu = 0.56 \cdot 10^6 \text{ cm}^2/\text{Vs}$, but with a very high carrier density of $8.5 \cdot 10^{11} \text{ cm}^{-2}$ [74]. In general, we must conclude from the data reported in literature [74, 6] that there is no clear tendency of more pronounced MIRO with higher mobilities. It seems like as the electron mobility is unable to capture the important sample aspects required to observe pronounced MIRO. It has been established that the displacement contribution to MIRO is highly sensitive to the disorder potential landscape.

In 2014 MIRO were discovered in SiGe heterostructures ($\mu > 4 \cdot 10^5 \text{ cm}^2/\text{Vs}$)

[37] as well as in ZnO heterostructures with electron mobilities as low as $\mu > 5 \cdot 10^4 \text{ cm}^2/\text{Vs}$ (this thesis). As these samples have higher carrier density compared to the ultrahigh mobility GaAs samples, this supports the tendency that high carrier densities are beneficial to observe MIRO [74, 6]. We refer to chapter 7 for a detailed analysis of whether the quantum lifetime and mobility correlate with the absence or presence of MIRO in ZnO heterostructures.

3.2.6 Effective mass

As shown by Hatke et al. MIRO provides a more accurate way to determine the effective mass of charge carriers [75], since the oscillation period depends on the cyclotron frequency. Conventionally, the effective mass is extracted from the temperature dependence of Shubnikov de-Haas (SdH) oscillations. However, this is more complicated, because in contrast to MIRO the position of SdH oscillations does not depend on the mass, but on the filling factors, which are independent of m^* :

$$\nu = \frac{hn}{eB} \quad (3.4)$$

Electron–electron interactions that cause a change in the effective mass can be probed with MIRO, although up to now this process is not fully understood. In GaAs this leads to a reduced effective mass of $m^* = 0.059 m_0$ instead of the commonly reported bulk value of $m^* = 0.067 m_0$ [76]. A study of the effective mass using MIRO has been carried out for ZnO in chapter 7.

3.2.7 Fractional MIRO

Fractional MIRO, where the microwave energy is lower than the cyclotron energy ($\hbar\omega_c > \hbar\omega$), have been observed in [45]. This effect is discussed either in terms of multi photon absorption via virtual states or sidebands or in terms of sequential absorption of several photons. For a detailed overview please refer to [40].

3.2.8 Zero resistance states (ZRS) and bistability

In experiments with samples that show pronounced MIRO, the change in resistivity can be as high as the resistivity drops all the way to zero. Both, the displacement and inelastic mechanism, assume that the electric system remains homogenous and the resistivity would drop below zero when the microwave-induced resistivity change is larger than the absolute resistivity. However, when the resistivity turns negative, the system is no longer stable and is unable to support a homogenous time-independent current flow. Instead it must break up in domains that carry currents with opposite directions even if no current is imposed through the sample. This spontaneous symmetry breaking due to domain formation has been theoretically addressed by Andreev et al. [77] as well as how this domain formation finally results in measurement of zero resistance in experiment. Hence, in order to account for the zero resistance state the displacement and inelastic models for MIRO need to be combined with domain formation due to an electronic instability as $\rho < 0$. These regions of zero resistivity are referred to as zero-resistance states (ZRS). A recent publication by Dorozhkin et al. [78] reports telegraph noise measurements in the ZRS regions as an experimental verification for the instability and domain formation.

3.3 Photovoltage / Photocurrent measurements

In 2009, S. Dorozhkin et al. [79] reported that two-dimensional electron systems subject to microwave radiation do not only induce oscillations in the resistivity, but also in the photovoltage and photocurrent signals. In the paper they used a sample with patterned contacts on the rim of the 2DEG (external contacts) as well as inside the 2DEG (internal contacts).

In Figure 3.6 these photocurrent and photovoltage oscillations are shown. The largest amplitude is realized, if an internal and an external contact are used for the measurement. Two external contacts give a signal which is 2 orders of magnitude smaller (compare curve at the bottom, marked with x100). All features move with frequency, according to the behavior discussed in the context of MIRO.

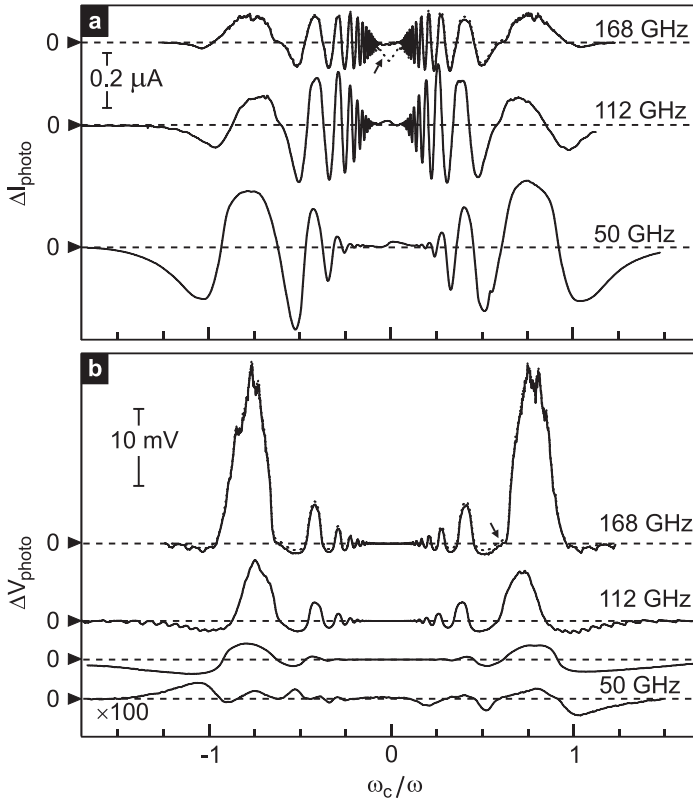


Figure 3.6: Photocurrent (a) and photovoltage (b) signals under constant microwave radiation as a function of magnetic field (plotted as a function of ω_c/ω the ratio of cyclotron to microwave frequency). All traces use a combination of an internal and external contact, except for the bottom one (multiplied by factor $\times 100$), which was recorded between two external contacts. (taken from [79])

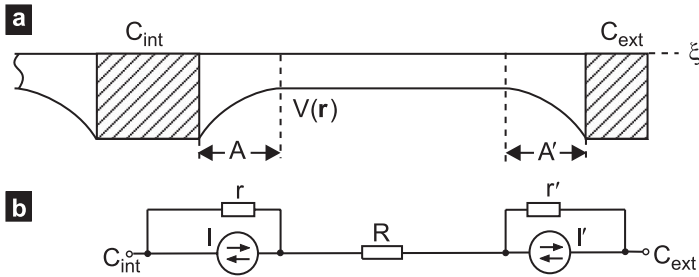


Figure 3.7: Equivalent circuit diagram to explain the appearance of photocurrent and photovoltage oscillations in a 2DEG under the influence of microwave radiation (adopted from [79])

In this thesis the photocurrent and photovoltage signals mentioned above are explained in terms of the displacement mechanism, although the non-equilibrium distribution function mechanism also provides a similar explanation [80]. The explanation based on the displacement mechanism is, however, more illustrative.

The displacement mechanism (see chapter 3.1.1) is based on Landau levels (LL), that are tilted by the current-induced Hall voltage. For photocurrent and photovoltage signals no current is imposed through the sample, yet the LL may still be tilted locally by built-in electric fields near the contacts, which originate from a difference in the work function of the 2DEG and the contact material. Electronic excitations that do not exactly match the cyclotron energy fulfill energy conservation by spatially displacing the electrons as illustrated in Figure 3.2 for LL tilted by the Hall electric field. Therefore a photocurrent will flow in the direction of the built-in electric field.

Figure 3.7 (a) shows the built-in electric fields near the contacts as well as the equivalent circuit (b) for this mechanism. Depending on the microwave detuning the current flow can be in the direction of the built-in electric field or opposite. This is depicted in the equivalent circuit with a pair of oppositely directed current arrows.

For an open circuit configuration a compensating current will flow across the shunt resistances in the areas A and A' to ensure that no net current will flow. Due to differences in shunt resistance of internal contacts, which are Corbino-like ($\sigma_{xx}^- \approx \rho_{xy}^2 / \rho_{xx}$), and external contacts which are proportional to ρ_{xx} , the measured photovoltage is much higher if an internal and an external contact are combined.

3.4 Polarization experiments

So far we have not considered the polarization of incident microwave radiation in our discussion of MIRO. For both theoretical models the polarization dependent Drude conductivity is a basic ingredient and contained in the amplitude prefactor A_ω in formula 3.2.

3.4.1 Circular polarization

Both, the inelastic and the displacement mechanism predict an influence of the polarization on the photoconductivity depending on the orientation of the circular polarization with respect to the magnetic field direction [40]. A publication by Smet et. al [81], so far the only circular polarization study for MIRO, does not find a significant difference in MIRO signal for both circular polarization orientations, as depicted in Figure 3.8.

However, controlling the polarization state inside an optical cryostat is difficult and it can not be experimentally proven that the microwave polarization is circular next to the 2DEG. On the one hand nearby metallic contacts may influence the polarization, as demonstrated in a calculation for a simplified geometry [82]. On the other hand absorption measurements show a clear difference between the two orientations near the cyclotron resonance. It is up to future experiments to prove the influence of circular polarization on MIRO which can be considered as one of the most important open questions to MIRO.

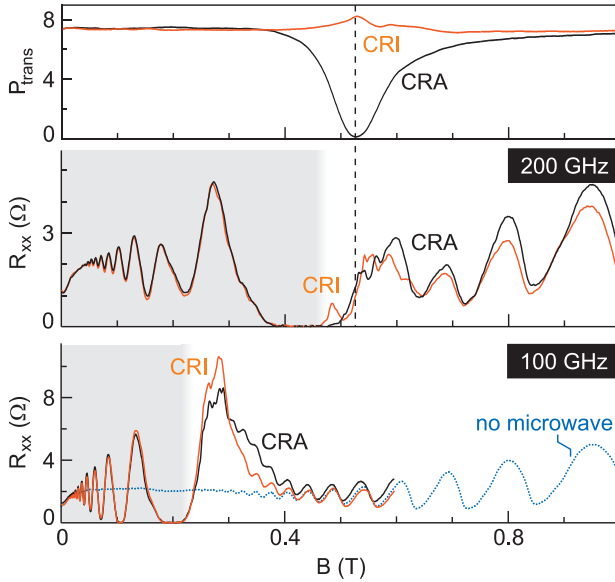


Figure 3.8: MIRO for different circular polarizations: cyclotron resonance active (CRA) and cyclotron resonance inactive (CRI effectively showing no influence of the polarization orientation for magnetic fields below the cyclotron resonance (shaded in gray). Microwave absorption data for 200 GHz (adopted from [81])

3.4.2 Linear polarization

So far equal strength of MIRO amplitude for linear polarizations along and perpendicular to the current direction are reported by multiple publications [32, 81, 83], although a publication by [84] is reporting a cosine dependence. This is in accordance with the combined theory of displacement and inelastic mechanism, if interpreted in the following way: As for the inelastic mechanism no MIRO amplitude dependence on the linear polarization direction is expected, experiments showing no linear polarization dependence are dominated by inelastic mechanism. This argument turned inside out means that a dependence on linear polarization indicates a contribution of the displacement mechanism. Temperature and power dependent measurement may help clarifying this issue in the future [40].

Part II

Experimental part: Microwave-induced quantum oscillations in ZnO

The following chapters deal with the observation of microwave-induced resistance oscillations (MIRO) and closely related photovoltage and photocurrent oscillations in ZnO heterostructures. It is the first report of MIRO and related effects in an oxide system¹. After the report in strained Ge/SiGe by Zudov et. al. [37], this work demonstrates MIRO in a third material system besides GaAs/AlGaAs heterostructures where they have been discovered in 2001 [31, 30]. This extends the range of materials and thus offers new playgrounds for experimentalists and theoreticians to verify and review the current understanding, that so far has been exclusively developed in GaAs systems.

Moreover, the discovery of MIRO in an oxide system allows for further exploration of the parameter space. Conduction band electrons in oxides are often d- and f-shell electrons. Therefore, oxides, such as ZnO, very often have much higher effective masses, compared to semiconductors e.g. ($m^*_{\text{ZnO}} \simeq 0.3m_e$ $m^*_{\text{GaAs}} \simeq 0.067m_e$). As a result, the cyclotron energy at a given magnetic field in ZnO is a factor of 4 smaller than in GaAs:

$$E_c = \hbar\omega_c = \hbar \cdot eB / m^* \quad (3.5)$$

$$E_c^{\text{GaAs}}[\text{meV}] = 1.73 \cdot B[\text{T}] \quad (3.6)$$

$$E_c^{\text{ZnO}}[\text{meV}] = 0.39 \cdot B[\text{T}] \quad (3.7)$$

Since the magnetic field position of MIRO is dependent on the effective mass, MIRO in ZnO are shifted to higher magnetic fields. Because of the higher g-factor in ZnO ($g_{\text{ZnO}} = 3.86$, $g_{\text{GaAs}} = -0.44$) [24] the cyclotron energy and Zeeman energy are comparable and the ratio is a factor of 40 bigger than in GaAs. Due to the larger Landé factors (g-factor) the ZnO material system offers the possibility to study spin effects in the context of MIRO.

In the following chapters MIRO in ZnO heterostructures will be demonstrated as well as their temperature and power dependence. Afterwards a comparison of quantum lifetimes show that MIRO can be used as a micro-

¹publication in preparation: D. F. Kärcher, Yu. A. Nefyodov, J. Falson, I. A. Dmitriev, S. I. Dorozhkin, D. Maryenko, Y. Kozuka, A. Tsukazaki, M. Kawasaki, A. V. Shchepetilnikov, I. V. Kukushkin, K. von Klitzing and J. H. Smet, Microwave-induced resistance oscillations in ZnO/MgZnO heterostructures

scope by comparing experiments that probe the quantum lifetime τ_q on different length-scales. Therefore in chapter 4 we will start with the microwave-induced resistance changes and demonstrate the occurrence of MIRO in ZnO heterostructures. To study temperature and power dependence gears will be shifted to photovoltage measurements, since it turns out that they provide a cleaner signal (chapter 5). In collaboration with the Institute of Solid State Research RAS², we studied MIRO on samples with different charge carrier densities. A summary of the combined results will be presented in chapter 6. Only samples with a minimum electron density in of $n = 3.9 \cdot 10^{11} \text{ cm}^{-2}$ to $n = 6.5 \cdot 10^{11} \text{ cm}^{-2}$ show MIRO signals, while samples with lower densities show cyclotron resonance absorption (CRA) covered in section 9. In Chapter 7 it will be demonstrated that MIRO can also be used to determine the quantum lifetime. We will test the quantum lifetime τ_q with three different methods: by analyzing the dampening of Shubnikov de-Haas oscillations, by analyzing the dampening of microwave-induced resistance oscillations and the photovoltage oscillations. These different methods address quantum scattering of electrons on different length-scales and hence may reveal the characteristic length-scales of the disorder landscape felt by the electrons.

The experiments involve the following parameter space:

- Magnetic field $B = -3 \text{ T} \dots +3 \text{ T}$
- Helium bath temperature $T_{\text{He}} = 1.35 \text{ K} \dots 10 \text{ K}$
- Microwave frequency $f_{\text{MW}} = 30 \text{ GHz} \dots 170 \text{ GHz}$
- Microwave output power $P_{\text{out}} = 0 \text{ mW} \dots 10 \text{ mW}$.
(P_{out} refers to the output power of the microwave source)

However, not all parameters can be controlled independently. The two major dependencies that influence the interpretation of the following measurements the most are the following:

1. The absorption of microwaves by the two-dimensional electron system causes an increase in the electronic temperature. This also translates to

²Institute of Solid State Physics RAS, 142432 Chernogolovka, Moscow District, Russia

an increase in the lattice temperature. As we increase the microwave output power P_{out} causes an increase in the electronic temperature T_{el} .

2. Due to the working principle of backward-wave oscillators (BWOs), which are used in the experiment to generate the microwaves, the frequency of the microwave f_{MW} cannot be tuned independent of the microwave output power P_{out} . Figure 3.9 gives an impression of the emitted microwave power as a function of frequency. Although the nominal output power is constant, one can see that changing the microwave frequency f_{MW} varies the output power P_{out} of the BWO by more than an order of magnitude. Moreover, the entire propagation stretch will cause strong interference at each given microwave frequency. Overall this gives rise to very different levels of incident power at the sample.

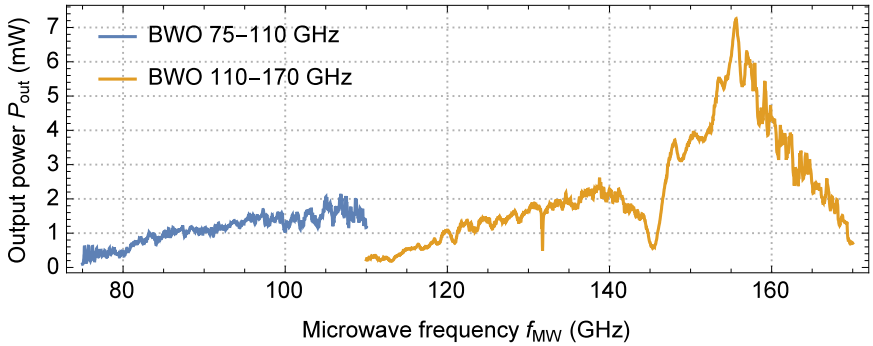


Figure 3.9: Fixed nominal power output of two backward wave oscillator (BWO) sources (75–110 GHz (blue), 110–170 GHz (orange)) as a function of the microwave output frequency. The emitted power changes by more than one order of magnitude due to the working principle of BWOs

Chapter 4

Microwave-induced resistance oscillations

Microwave-induced resistance oscillations (MIRO) show up as an oscillation of the magnetoresistance, additionally to Shubnikov de-Haas oscillations, when the sample is irradiated with microwaves. In this thesis we report the occurrence of MIRO in ZnO, as a first material system to push the MIRO boundary into the world of oxides. Figure 4.1 shows the longitudinal resistance vs. magnetic field traces with (orange) and without (blue) incident microwave radiation. One can clearly see an increase in the resistance around ± 1.5 T, a decrease around ± 1 T and a node in-between corresponding to $\omega_c = 2\pi f_{MW}$.

In the following the MIRO extrema are denoted by their affiliation to a specific ϵ_{ac} , marked by + for a maxima and - for a minima (e.g. the maxima which is close to $\epsilon_{ac} = 2$ is called MIRO 2+ feature).

Especially the resistance decrease of the MIRO 1- feature is a validation for MIRO, since for a material with metallic behavior a resistance decrease cannot be explained by heating effects (induced by the microwave radiation), which would increase the resistance. The resistance difference (green) shows additional MIRO features, like 2+, 2- and maybe 3+.

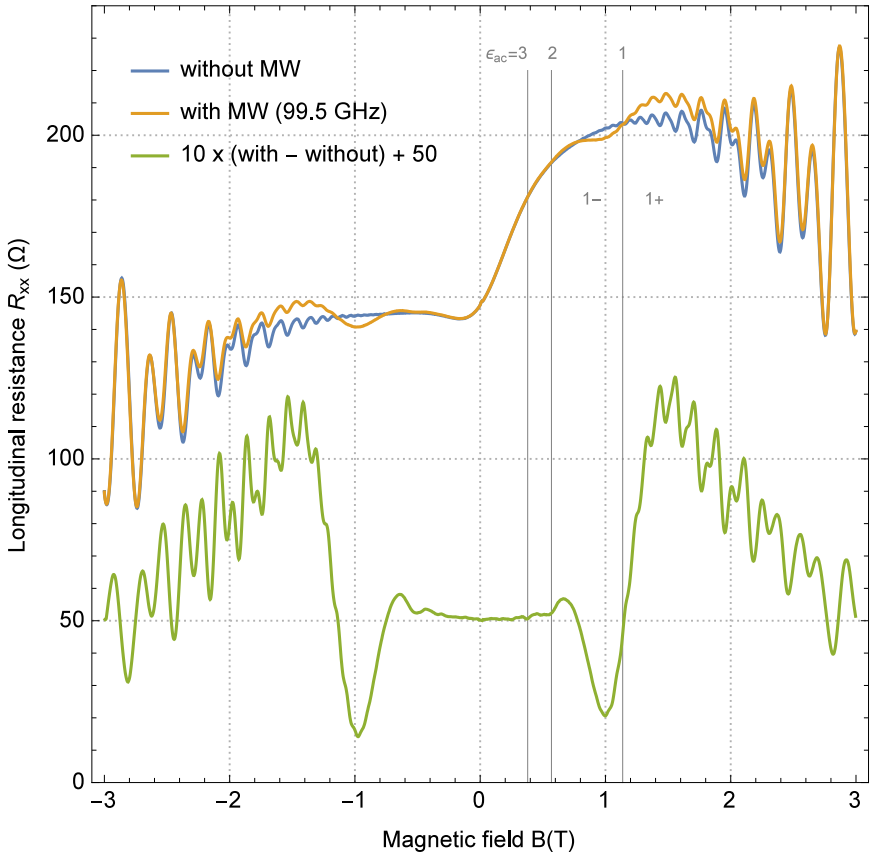


Figure 4.1: MIRO raw data: magnetoresistance traces with (orange) / without (blue) microwave radiation show a clear resistance difference around ± 1 T and ± 1.5 T. They can be associated to the MIRO 1+ and 1- extrema. The difference in resistance is multiplied by a factor of 10 for clarity (green). For comparison magnetic field values, which correspond to the ratio of microwave energy to cyclotron energy $\epsilon_{ac} = 1, 2, 3$, are drawn as vertical lines

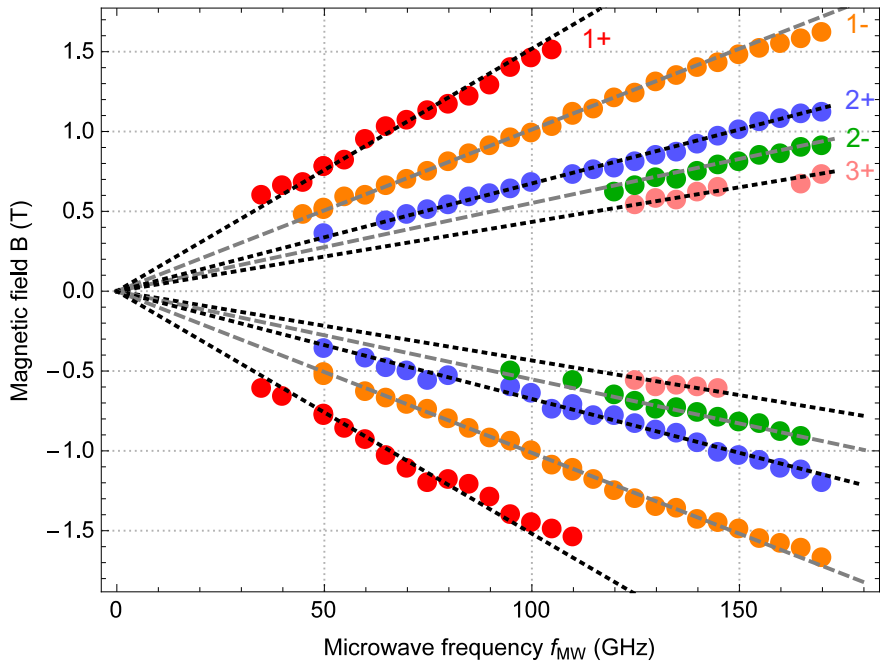
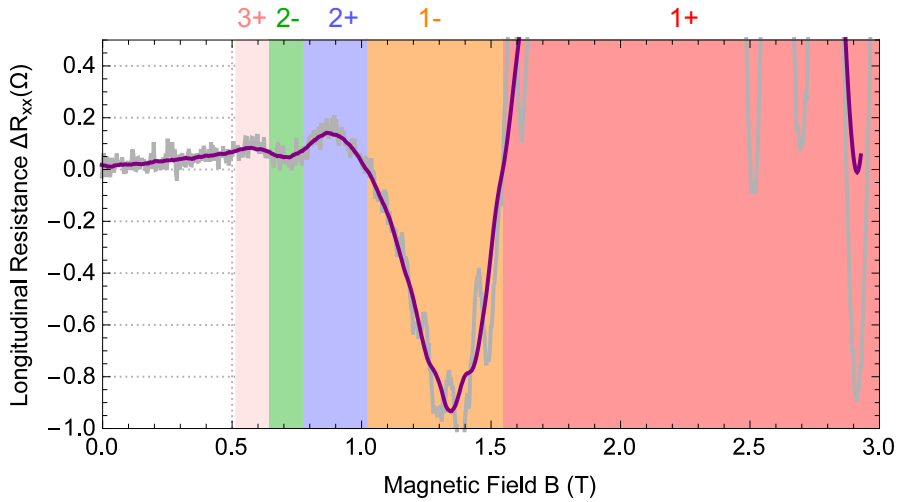
The experiment has been performed in a van der Pauw device with 8 contacts, thereof 4 at the edges and 4 in the middle of the sides (we refer to Figure 7.5 on page 84 for a scheme). The asymmetric behavior of the resistance with respect to zero magnetic field, i.e. the strong increase in resistance for positive magnetic fields, which is absent for negative fields, is caused by inhomogeneities in the sample, which are probed by different current paths for different field polarities. Different voltage probe pairs show a variety of step like and v-shaped traces for the longitudinal resistance. This aspect is not affected by microwave radiation and can be treated independently.

4.1 Frequency dependence

The experiment displayed in Figure 4.1 is repeated for different frequencies within the range of 30 to 170 GHz using two different microwave sources. For the low-end frequency range a signal generator is used, while higher frequencies are generated with a backward wave oscillator (BWO) at 3 different insets:

- 30 ... 50 GHz: Agilent 83650B signal generator
- 50 ... 75 GHz: ELVA 1 G4-134ce 50-75 BWO
- 75 ... 110 GHz: ELVA 1 G4-134ce 75-110 BWO
- 110 ... 170 GHz: ELVA 1 G4-134ce 110-170 BWO

The lower frequency limit stems from the visibility of MIRO in ZnO, while the upper limit is set by the availability of microwave sources. Figure 4.2 (top) shows a representative magnetoresistance curve with MIRO features up to 3+, indicated by different background colors. MIRO maxima and minima are determined for the different frequencies and plotted separately in the frequency vs. magnetic field plane (bottom). The magnetic field positions of MIRO extrema show a linear dependency as a function of the microwave frequency. This is expected, as the cyclotron energy $\hbar\omega_c = eB/m^*$ increases linearly with the magnetic field and also the microwave photon energy $\hbar\omega = \hbar 2\pi f_{\text{MW}}$ increases linearly with frequency.



The MIRO minima and maxima are fitted well with the formula

$$\omega_{\min/\max} = (i \pm \phi_i) \omega_c, \quad i = 1, 2, 3, \dots \quad (4.1)$$

where m^* and ϕ_i are treated as fitting parameters. One obtains $m^* = 0.34$ and $\phi_i = 0.2$. For strongly overlapping Landau levels (LL) and MIRO features with $\epsilon_{ac} > 3$ one would expect a $\phi_i = 0.25$, described as a harmonic oscillation in equation 3.2. The fitting result of $\phi_i = 0.2$ can be explained by taking also MIRO 1+,1-,2+,2- features into account - these features are shifted towards integer values of $\epsilon_{ac} = \omega/\omega_c$, because LL start to separate. Therefore the interpretation of m^* is more difficult and less meaningful. A more accurate determination of m^* can be achieved by an analysis of the nodal points, as done for the temperature dependent photovoltage data in chapter 5.1 or in the framework of the analysis of the quantum lifetime in chapter 7.

Because MIRO signals are small in ZnO, the microwave power is a crucial factor. The following experiments are done with maximum output power, but the microwave intensity at the sample is not constant upon changing the frequency due to three reasons:

- Due to the working principle of backward wave oscillators (BWO) their output power varies strongly with frequency (see Figure 3.9) .
- An oversized rectangular waveguide is used to transmit the microwave to the sample. Due to inevitable mode conversion, the damping factor of this waveguide is frequency dependent
- The sample is placed inside a sample rod surrounded by a metal housing and metal electrodes are used for electrical contact. Depending on the frequency different standing waves build up and hence the microwave

Figure 4.2 (*preceding page*): Magnetoresistance trace under microwave radiation ($f = 135$ GHz) with colored background, corresponding to different MIRO features (top). RAW data shown in gray; 100 mT moving average shown in purple. Magnetic field position for different MIRO features and varying microwave frequency show a linear dependence (bottom). The straight lines are a best fit to the data and yield $m^* = 0.34$ and $\phi_i = 0.2$.

power at the 2DEG varies with the frequency. This was double checked using an external E-H-Tuner. Leaving the nominal power and frequency constant one can increase and decrease MIRO amplitudes by using an E-H-Tuner. This is plausible, because the E-H-Tuner changes the relative phases of electric and magnetic field components and therefore affects the standing microwaves.

The varying microwave power leads to a varying MIRO amplitude and observability of different MIRO features across the frequency spectrum explaining the experimental gaps of the fitted minima and maxima in Figure 4.2. The MIRO 1+ feature could not be resolved for magnetic fields higher than 1.5 T, because of the strong influence of Shubnikov de-Haas oscillations.

Nevertheless, the provided data show a clear linear behavior as expected from theoretical models. This confirms unequivocally that it is MIRO in ZnO which we observe. In the next section we turn our attention to the photovoltage and photocurrent.

Chapter 5

Photovoltage & Photocurrent measurements

In order to investigate microwave-induced photovoltage oscillations (MIPVO) in ZnO heterostructures, samples are fabricated with additional internal contacts (refer to Figure 7.5 on page 84 for the measurement scheme).

Photovoltage and photocurrent signals are strongest when measuring between an internal and an external contact (also refer to section 3.3 for an explanation of the mechanism that governs MIPVO). Experimentally it will turn out that photovoltage signals can be more easily detected and show more features than MIRO. Hence photovoltage experiments will be used to analyze the temperature (section 5.1) and power (section 5.2) dependence of the microwave induced oscillations. The photovoltage measurements will also be used to extract electron quantum lifetimes τ_q . They will be compared with values obtained from MIRO (section 7).

Figure 5.1 shows a comparison of MIRO, photovoltage and photocurrent signals as a function of the applied perpendicular magnetic field. Microwave

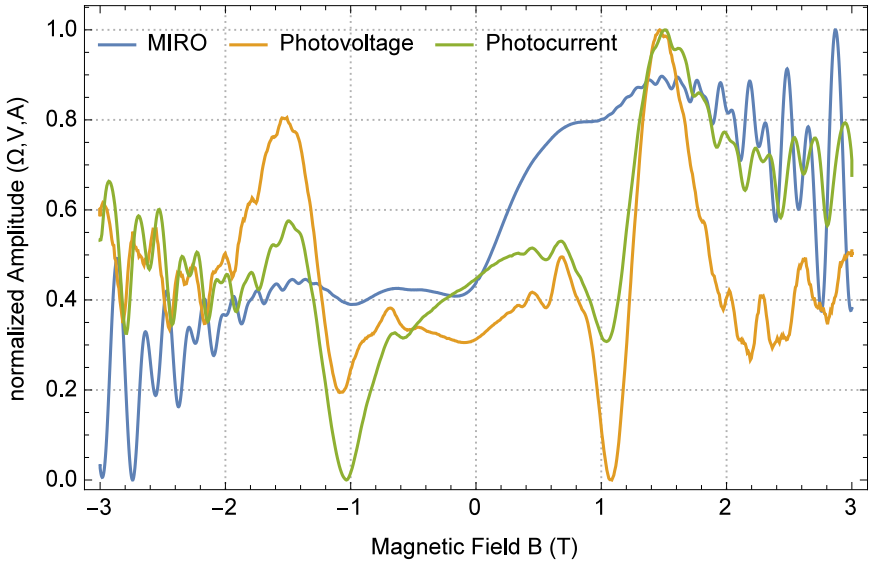


Figure 5.1: Comparison of magnetoresistance, photovoltage and photocurrent signals versus magnetic field under microwave radiation $f = 106.7$ GHz. Signals are normalized to an amplitude of 1 within a field range of ± 3 T.

radiation with a fixed frequency of $f = 106.7$ GHz is applied to the sample. All signals are normalized so that the lowest value of a curve corresponds to 0 and the highest value to 1. Obviously, microwave-induced oscillations are much better visible in the photovoltage and the photocurrent. Here extrema up to the MIPVO 4+ are visible and the amplitude, compared with Shubnikov de-Haas oscillation features, is significantly increased.

For photovoltage and photocurrent measurements one and the same sample with identical contact configuration was used, while the resistance data was recorded on another sample from the same wafer, but without internal contacts. This was done, because recording resistance traces with microwave radiation on samples with internal contacts leads to weaker and often unusual signals. This can be attributed to the disturbing influence of internal contacts on the current flow.

Photovoltage and photocurrent signals are recorded by modulating the microwave intensity. In the case of photocurrent we convert the signal into a voltage signal using a current preamplifier (Ithaco 1211). Subsequently, a lock-in amplifier detects the voltage at the microwave modulation frequency. The resistance trace is measured with constant microwave radiation using a modulated current instead.

Internal & external contacts

Internal contacts were fabricated by evaporating Ti/Au circles with the help of a shadow mask (diameter is $360 \mu\text{m}$, separation $120 \mu\text{m}$). Additional contacts around the rim of the sample were soldered with Indium to obtain a van-der-Pauw geometry. Afterwards ultrasonic wire bonding on top of the internal contacts was used to connect to the pads of a chip carrier. This helps to break through the MgZnO top layer and contact the 2DEG.

Figure 5.2 displays a comparison of the 2-terminal resistance change of internal (Corbino-like) contacts and external (edge-like) contacts as a function of the magnetic field. The resistance traces are normalized to 1 for zero magnetic field. While the edge-contact shows only a weak magnetoresistance, the Corbino-like resistance changes by more than an order of magnitude. Within the framework of compressible and incompressible stripes the observed behav-

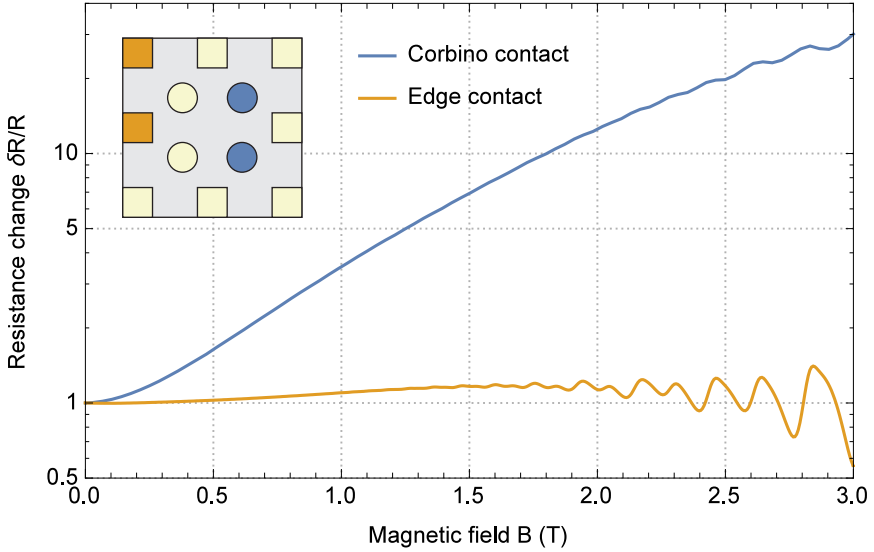


Figure 5.2: Comparison of corbino-like (blue) and edgetype-like (orange) contact resistance as a function of magnetic field. Resistances are normalized to 1 for $B=0$. Shown is the 2-terminal resistance change between a pair of internal (corbino-like) contacts (blue) and external (edge-like) contacts (orange). The inset shows a schematic of the sample in van-der-Pauw geometry with 4 internal contacts.

ior can be explained: Edge contacts enforce equilibration since the current carrying incompressible strips must enter them. Corbino-like contacts however are isolated because incompressible stripes run around them but do not enter. The isolation gets stronger with increasing magnetic field.

The contact resistances come into play as shunt resistances in the formation of the MIPVO signal. The difference in the shunt resistance of an internal and an external contact increases the MIPVO signal (as discussed in section 3.3).

5.1 Temperature dependence

In this section the temperature dependence of MIPVO will be discussed. The temperature dependence is primarily studied for two reasons: First it resembles the temperature behavior expected from temperature dependent studies on GaAs heterostructures, which are covered in theory by the displacement and inelastic mechanism. Therefore it further strengthens the interpretation of the data as MIRO in ZnO heterostructures. Second, the temperature dependence allows to distinguish the importance of displacement and inelastic mechanism in ZnO.

The temperature is controlled with the help of a variable temperature inset (VTI). Temperature stability for all temperatures was better than 50 mK and was monitored with a Cernox temperature sensor. Helium gas is sucked in the VTI through a heat exchanger. Setting different temperatures to the heat exchanger preheats the gas to different temperatures. Figure 5.3 shows magnetoresistance traces for different temperatures. One can see that the MIPVO signal disappears when the temperature is gradually raised from 1.5 K to 10 K.

The photovoltage changes significantly with temperature, except close to the nodal points at 0.8 T and 1.25 T, where all traces pass the same point. Only two nodal points can be seen clearly, because the other nodal points, which should occur between integer values of $\epsilon_{ac} = \omega/\omega_c$, are affected by the temperature-dependent background. The nodal points allow for a precise determination of the electron effective mass. We obtain $m^* = 0.33 \pm 0.002m_e$. Between the integer values of $\epsilon_{ac} = 1 \dots \epsilon_{ac} = 2$ another nodal point shows up. As evident from the formula in section 3.2 (page 35) this nodal point should lie

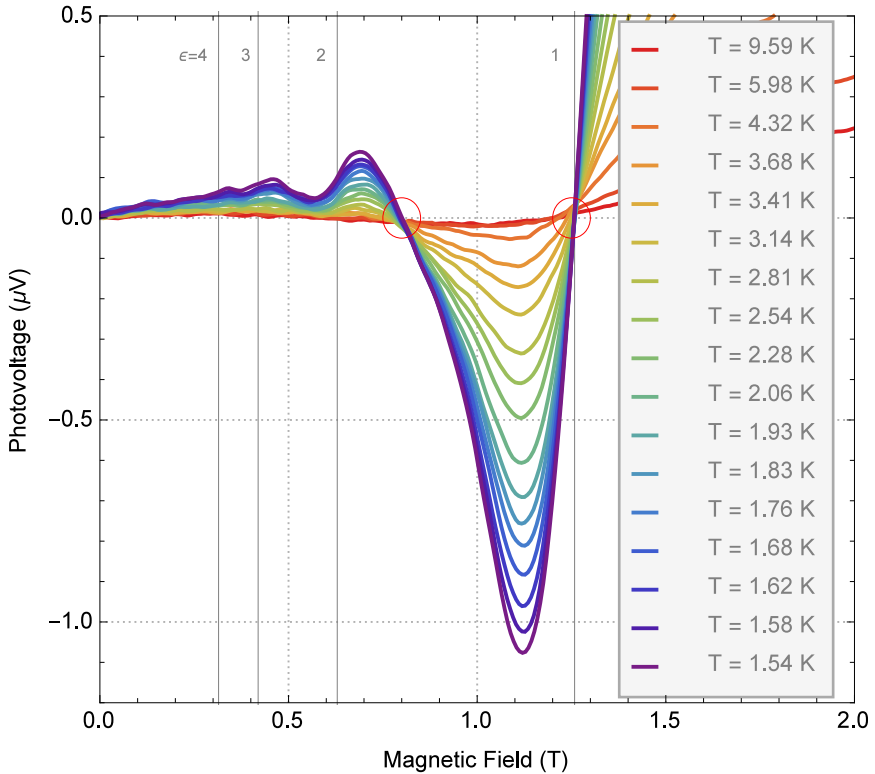


Figure 5.3: Temperature dependent MIPVO signals, as a function of the magnetic field, show photovoltage oscillations up to the 4+ feature. The transitions from 1- to 1+ and 2+ to 1- clearly show nodal points (red circles). Using the effective mass of $m^* = 0.33 m_0$, magnetic field values corresponding to integer values of $\epsilon_{ac} = \omega/\omega_c = 1, 2, 3, 4$ are indicated by vertical lines.

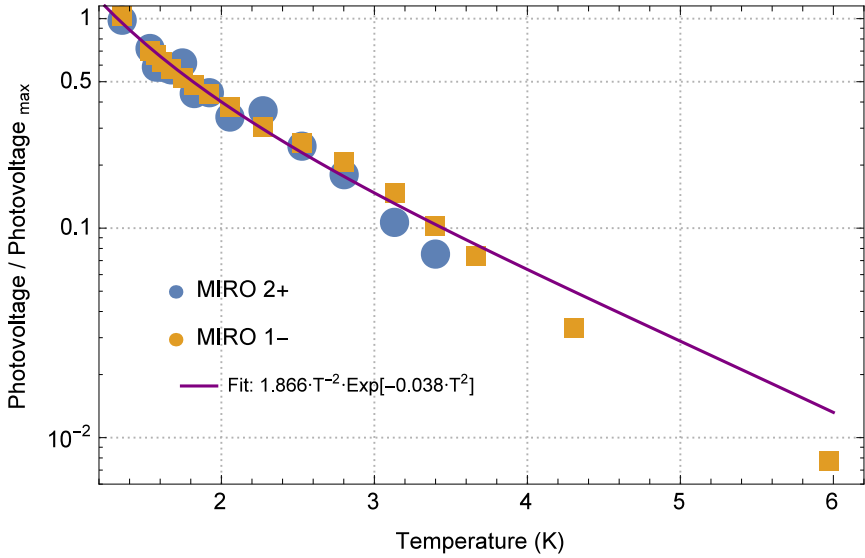


Figure 5.4: Temperature dependent MIPVO analysis based on the data shown in Figure 5.3. Only the two strongest and well defined features 1- and 2+ are used for the analysis. The fitting function has both a logarithmic and a square temperature dependent contribution in the examined range indicating a contribution from both the inelastic and the displacement mechanism.

exactly at $\epsilon_{ac} = 1.5$. In Figure 5.3 one can see that this nodal point is shifted towards $\epsilon_{ac} = 2$. This indicates that LL no longer strongly overlap, but start to separate.

To extract the temperature dependent amplitude of the MIPVO signal, a background subtraction is necessary. This was done as follows: A polynomial function was constructed that passes through the data points at $B=0$ and where ϵ_{ac} takes on integer values 1...4 (hereby we have used $m^* = 0.33$ as the effective mass, as extracted before from the analysis of the magnetic field position of the nodal points. MIRO extrema were extracted for the two strongest MIRO features 1- and 2+ and normalized to 1 for the lowest available temperature ($T=1.35$ K (not shown in Figure 5.3)). The MIRO 1+ maximum is not suitable because it interferes with Shubnikov de-Haas oscillations.

The normalized MIPVO amplitudes as a function of temperature (shown in Figure 5.4) are fitted with the following function, that describes both, the inelastic and displacement contributions:

$$\delta\rho_{\omega}(T)/\delta\rho_{\omega}(T_0) \propto A(d + (1 - d)T^{-2}) \exp(-bT^2). \quad (5.1)$$

Here T is the temperature, A is an amplitude prefactor, d is the relative contribution of the displacement mechanism (while $1 - d$ is the contribution from the inelastic mechanism) and b the contribution of LL broadening introduced by electron-electron interaction, which lowers the quantum lifetime $1/\tau_q^*(T) = 1/\tau_q + \alpha T^2$. The fitting reveals, that the inelastic mechanism dominates ($d = 0$) within the accuracy of the data. With $d > 0.1$ the fitting diverges significantly from the measured data.

Experiments in a dilution fridge

Additional experiments, carried out in a dilution refrigerator at lower temperatures (< 300 mK) did not reveal a deeper insight in the MIPVO temperature dependence, because of two reasons: First, due to the material properties of the rectangular waveguide in the dilution fridge, the transmitted microwave power is reduced significantly and therefore the amplitudes of MIRO and MIPVO are very small. Second, Shubnikov de-Haas oscillations are more pronounced at lower temperatures, and therefore mask the MIRO and MIPVO signals.

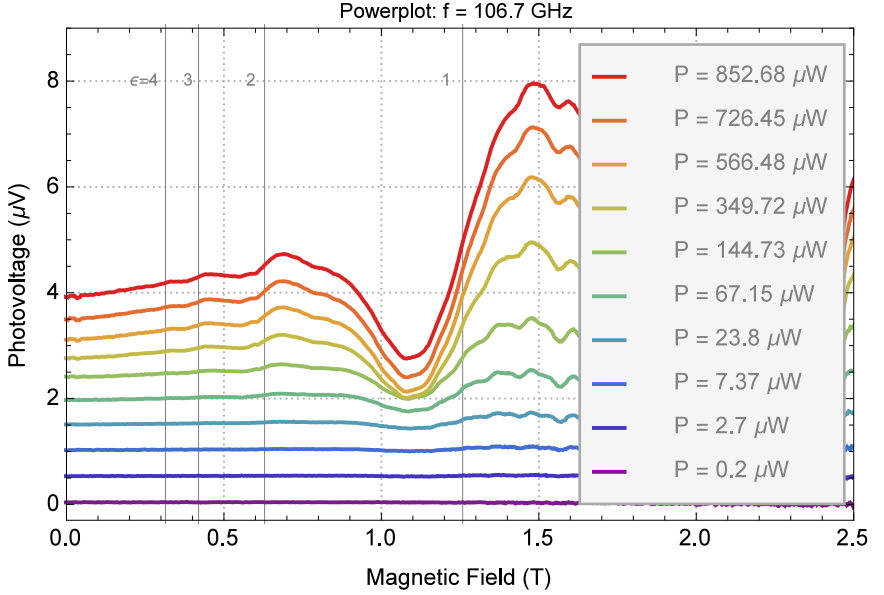


Figure 5.5: Power dependence of the MIPVO signal for a fixed frequency of $f = 106.7$ GHz. The different traces are offset by $0.5 \mu\text{V}$ for clarity. Using an effective mass of $m^* = 0.327$ magnetic field values corresponding to integer values of $\epsilon_{ac} = \omega/\omega_c = 1, 2, 3, 4$ are indicated by vertical lines.

5.2 Power dependence

The following section is intended to investigate power dependence of MIPVO signal amplitude. It will turn out that power dependence is very similar as expected from GaAs heterostructures. This will prove that the microwave power level is not yet high enough to cause saturation. In that regime, heating effects are more dominant than nonlinear transport due to microwave radiation.

Figure 5.5 shows magnetoresistance traces under the influence of microwave radiation ($f = 106.7$ GHz) for different power levels. The microwave radiation heats up the electronic system and therefore changes the background of the

magnetoresistance traces. A background subtraction that uses an interpolated curve identical to the trace at $B = 0$ and the magnetic field values where $\epsilon_{ac} = \omega/\omega_c = 1, 2, 3, 4$ enables us to focus on the MIPVO only.

The power is varied more than 3 orders of magnitude using a current driven microwave attenuator. Power values are recorded at the input of the waveguide integrated into the sample holder. The actual power level reaching the sample may deviate substantially from these values. The analysis will focus on relative values, which however remain despite losses and attenuation.

A nodal point analysis similar to the one done for temperature dependent measurements can be applied here, revealing an electron effective mass of $m^* = 0.327 \pm 0.002$. This value is in good agreement with the one obtained by the nodal point analysis of the temperature dependent data in section 5.1 ($m^* = 0.33 \pm 0.002$).

Figure 5.6 shows a log-log-plot of the MIPVO 1- amplitude vs. microwave power. Around $220 \mu\text{W}$ a clear transition from linear to sub-linear behavior can be seen. Colored stripes are drawn as a guide for the eye corresponding to linear (green) and square-root (magenta) behavior with power.

The transition from a P to a $P^{1/2}$ dependence is also known from GaAs heterostructures (refer to section 3.2.2) and can be interpreted as an additional proof for the occurrence of MIRO / MIPVO in ZnO heterostructures.

Since the power attenuator can have an influence on the microwave distribution within the waveguide, one needs to exclude misleading changes of the microwave field distribution around the sample when changing the attenuator transmittance. Therefore the experiment was repeated without the attenuator by changing the microwave power inside the microwave source. The power output cannot be suppressed as much as with the attenuator, hence no data below $50 \mu\text{W}$ (0% Output power) can be achieved. As can be seen in Figure 5.6 both data sets agree very well, leading to the conclusion that the microwave power, as seen by the sample, is proportional to the power at the entrance of the waveguide, guiding the radiation to the sample.

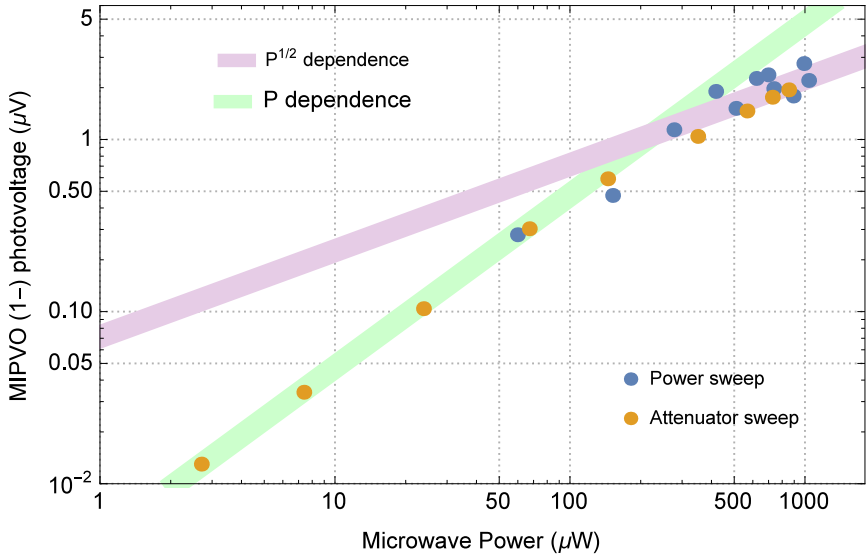


Figure 5.6: Power dependent MIPVO analysis based on the data shown in Figure 5.5 and a second dataset. Only the strongest and well defined 1- feature is used for the analysis. The colored bars show linear and square-root dependencies.

Chapter 6

Density dependence

In the course of our search for MIRO in ZnO samples we have examined samples covering densities ranging from $1.45 \cdot 10^{11} \text{ cm}^{-2}$ to $10.5 \cdot 10^{11} \text{ cm}^{-2}$. This work has been done in collaboration with the Institute of Solid State Research RAS¹. In this chapter we summarize the experimental findings of these density dependent measurements.

The electron density in ZnO heterostructures can be varied, by modifying the magnesium (Mg) content in the $\text{Mg}_x\text{Zn}_{1-x}\text{O}$ cap layer. A change in the Mg content has implications for the electron mobilities as discussed in chapter 2. Table 6 provides an overview on the different samples used for this thesis. As one can see the electron mobility changes by an order of magnitude from $500,000 \text{ cm}^2/Vs$ to below $50,000 \text{ cm}^2/Vs$ as the magnesium content is changed from 0.5% to 7%.

The onset of microwave induced resistance oscillations (MIRO) respectively microwave induced photovoltage oscillations (MIPVO) lies in between $3.9 \cdot 10^{11} \text{ cm}^{-2}$ and $6.5 \cdot 10^{11} \text{ cm}^{-2}$. It is interesting to see that the occurrence of MIRO is accompanied by the disappearance of cyclotron resonance absorption

¹Institute of Solid State Physics RAS, 142432 Chernogolovka, Moscow District, Russia

$n[10^{11} \text{ cm}^{-2}]$	Mg content [%]	$\mu[\text{cm}^2/\text{Vs}]$	MIRO/MIPVO	CRA
1.45	0.5	530,000	no	yes
2.05	1	290,000	no	yes
2.2	1	150,000	no	yes
3.9	3	80,000	no	yes
6.5	4.5	50,000	yes	no
8.5	5.5	50,000	yes	no
10.5	7	40,000	yes	no

Table 6.1: Overview of the ZnO/MgZnO heterostructures investigated and the experimental outcome for the microwave-induced resistance oscillations (MIRO) and cyclotron resonance absorption (CRA)

(CRA)². It is unclear if the appearance of MIRO and disappearance of CRA are linked to the same physical origin in ZnO.

The tendency that higher charge carrier densities lead to more pronounced MIRO is known from GaAs samples [6]. In the ZnO samples the higher electron densities are accompanied by a substantial drop of the electron mobility. Compared to other material systems the ZnO heterostructure used in this thesis are by far the electron system with the lowest electron density, where MIRO have been reported. This further strengthens the tendencies found on GaAs systems, which state that MIRO amplitudes are not directly correlated with the electron mobility [6].

²CRA will be discussed in chapter 9

Chapter 7

Comparison of the quantum lifetime extracted by SdH, MIRO and MIPVO

The observation of MIRO in ZnO heterostructures is somewhat surprising, keeping in mind that only the cleanest high-mobility GaAs heterostructures show MIRO. Usually electron mobilities of $> 10^6 \text{ cm}^2/\text{Vs}$ are required to see MIRO in GaAs, while for the ZnO heterostructures, as the ones examined in this thesis, electron mobilities are at least by one order of magnitude lower (please refer to table 6 in the previous chapter).

Apart from the electron mobility, the quantum lifetime of the electrons may play a role for MIRO. The purpose of this chapter is to investigate the quantum lifetime τ_q of the electrons in ZnO heterostructures. The values will be extracted using different methods as listed below. It will turn out that quantum lifetimes as high as $\tau_q^{\text{ZnO}} = 5 \text{ ps}$ are observed. This value compares very well to $\tau_q^{\text{GaAs}} = 6 \dots 20 \text{ ps}$ extracted in GaAs samples, which show MIRO [6].

We will use 3 complementary approaches to extract τ_q :

1. The dampening of the Shubnikov de-Haas oscillations amplitudes are analyzed in a Dingle plot to extract $\tau_{q, \text{SdH}}$ (section 7.1)
2. The relative amplitudes of different MIRO extremas (e.g. $1-, 2+, 2-, 3+ \dots$) for different frequencies are analyzed in an empirical fitting to extract the quantum lifetime $\tau_{q, \text{MIRO}}$ (section 7.2)
3. The relative amplitudes of different photovoltage extrema (e.g. $1-, 2+, 2-, 3+, 3-, 4+, \dots$) for different frequencies are analyzed in an empirical fitting to extract the quantum lifetime $\tau_{q, \text{MIPVO}}$ (section 7.3)

In section 7.4 the different quantum lifetimes from Shubnikov de-Haas $\tau_{q, \text{SdH}}$, MIRO $\tau_{q, \text{MIRO}}$ and photovoltage oscillations $\tau_{q, \text{MIPVO}}$ will be compared and discussed.

7.1 τ_q from Shubnikov de-Haas oscillations

This section analyses the Shubnikov de-Haas (SdH) amplitudes as a function of the magnetic field. The amplitudes of the extrema will be used to extract the quantum lifetime $\tau_{q, \text{SdH}}$ in a Dingle plot. For details concerning the Dingle plot analysis please refer to section 1.5.

Figure 7.1 shows an example of the longitudinal resistance R_{xx} (blue) as a function of the applied perpendicular magnetic field. SdH oscillations start from $B=1$ T. The magnetoresistance trace has an asymmetric background. It is found on all samples, but the shape changes as the sample or contact configuration is changed. In general, the asymmetric background is attributed to the details of the current distribution, which is modified when applying a magnetic field. The sample is measured in a van der Pauw geometry and hence the current is injected from point-like contacts. Therefore the current flow is not exactly defined (compared to a Hall bar geometry).

In order to extract the amplitude of the Shubnikov de-Haas oscillations a background subtraction is needed. Therefore a function is constructed with the help of interpolation points. They are determined in two different ways for high and low magnetic fields. For low magnetic fields ($B < 800$ mT) no SdH

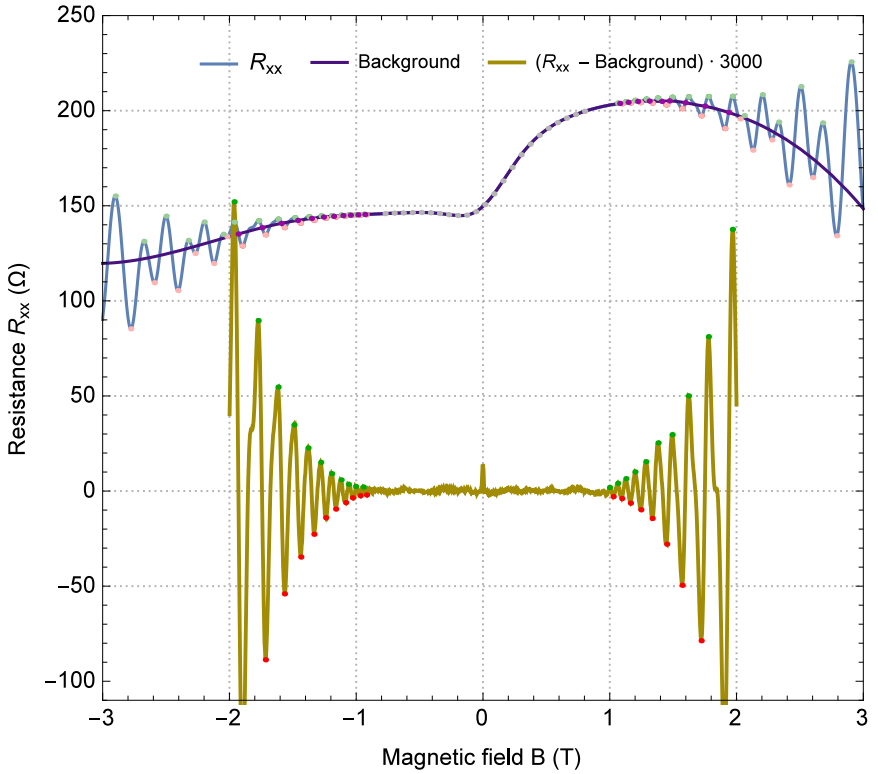


Figure 7.1: Shubnikov de-Haas oscillations with background subtraction

oscillations are present and 20 equidistant data points (gray) are selected to generate a smooth function. For strong magnetic fields ($B > 800$ mT) minima (light red) and maxima (light green) are fitted. Afterwards points are calculated that lie in the center of two neighboring extrema. These are taken as interpolation points (purple) for the smooth background function. Higher magnetic fields ($B > 2000$ mT) are excluded from this analysis, because of complications due to the onset of spin-splitting. The interpolation function is then subtracted from the longitudinal resistance and plotted with a magnification of 3000 (gold). The amplitude of minima (red) and maxima (green) are then extracted together with the magnetic field values.

The resistance peak at $B=0$ can be attributed to weak localization effects [85] and is not analyzed further here.

In Figure 7.2 the absolute resistance values of the extrema are plotted as a function of $1/B$ with the following formula (Dingle plot):

$$\ln\left(\frac{\Delta R}{4R_0} \cdot \frac{\sinh(A_T)}{A_T}\right), \quad \text{with} \quad A_T = 2\pi^2 k_B T / \hbar \omega_c \quad (7.1)$$

When fitting a linear function through the data points, the slope can be interpreted as $-\pi/(\omega_c \tau_{\text{textureq, SdH}})$. Using an effective mass of $m^* = 0.3 m_e$ a quantum lifetime of $\tau_{q, \text{SdH}} = 0.29$ ps can be extracted.

In MIRO experiments a higher effective mass, than assumed here, was found. Using this electron effective mass of $m^* = 0.33 m_e$, which enters ω_c and A_T , changes $\tau_{q, \text{SdH}}$ to 0.30 ps. This shows that the resulting $\tau_{q, \text{SdH}}$ is quiet robust to variations of the electron effective mass of 10%. We note that for the comparison of the quantum lifetimes in section 7.4, the exact values are of minor importance.

7.2 τ_q from MIRO

In the following section we analyze the relative amplitudes of different MIRO extrema to extract the quantum lifetime $\tau_{q, \text{MIRO}}$. The development of this method was an iterative process and is developed as part of this thesis. The same analysis is used for photovoltage extrema in section 7.3.

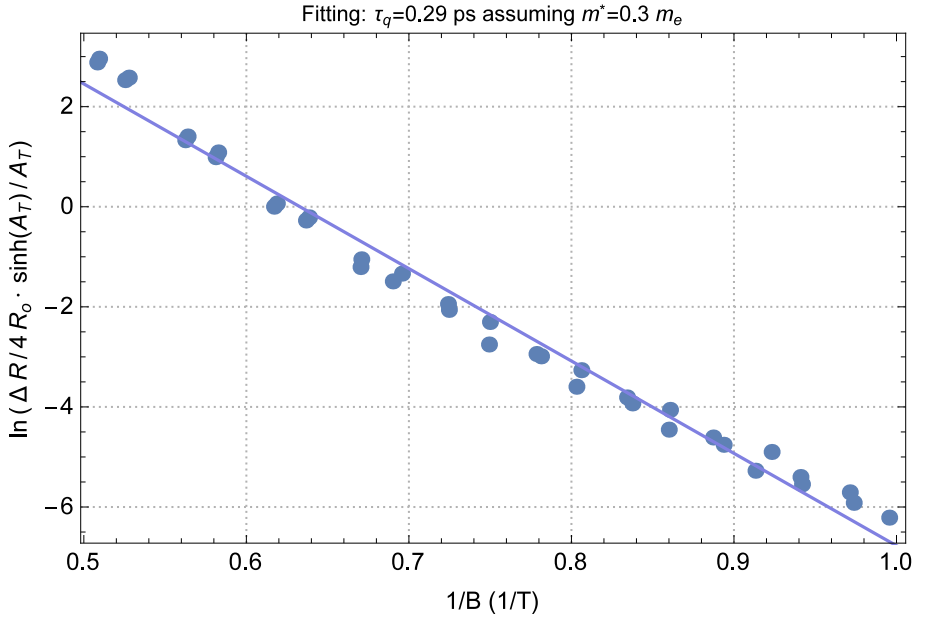


Figure 7.2: Dingle plot for the Shubnikov de-Haas oscillations (after background subtraction)

The idea of this analysis is to plot the recorded data in a way that MIRO oscillations show up as the absolute values of a cosine oscillation ($\sim |\cos|$). This requires to assume specific values for the quantum lifetime τ_q and the electron effective mass m^* . These values are varied in order to find the best fit. To present the precision of the fit, τ_q and m^* will be varied around, what was found to be the optimal value. The corresponding plots, that deviate with respect to the optimal one (a deviation from a $|\cos|$), will make the error analysis plausible. Additionally, it will show the robustness of the fitting method and hereby confirms the fitting.

As it will turn out, this approach provides very good results, especially if the noise level in the original dataset is very high. The recipe of the analysis will be presented in 4 steps:

The starting point for the analysis is a resistance difference signal, which was obtained by subtracting two magnetoresistance curves, with and without microwave radiation, from each other: $\delta R = R_{\text{MW}} - R_{\text{dark}}$.

- Plot the magnetoresistance as a function of ϵ_{ac} , which is dependent on the cyclotron energy ω_c and therefore a function of the electron effective mass m^* . This translates the $1/B$ oscillation in a harmonic representation.
- Remove the resistance background by subtracting an interpolation function. Values of the magnetoresistance trace at integer ϵ_{ac} points serve as interpolation points. Therefore by subtracting the interpolation function these points will be shifted to zero. This is motivated by the MIRO mechanism, that assumes no resistance change at integer ϵ_{ac} .
- Compensate for the MIRO decay by multiplying each curve with the inverse dampening factor: $\sum_{\pm} ((1 \pm \epsilon_{\text{ac}}^{-1})^2 + \beta^2) \exp(\alpha_q \epsilon_{\text{ac}}) \epsilon_{\text{ac}}^{-1}$, with $\beta \propto \gamma_{\text{eff}}/\omega$, with $\gamma_{\text{eff}} \propto \gamma + \tau^{-1} = 0.2 \text{ ps}$. This is dependent on both, the effective mass m^* , which enters the cyclotron energy, and the quantum lifetime $\tau_{\text{q, MIRO}}$, which enters α_q .
- Add up all frequencies (110 to 170 GHz), positive and negative magnetic fields and plot the absolute value. This projects all MIRO extrema onto each other and makes it easy to compare the height of different amplitudes.

As a result, one expects to see the absolute of the bare cosinusoidal MIRO oscillation. Two aspects are interesting to pay attention to.

1. Due to the dampening correction of the MIRO signal all oscillation amplitudes should be equal in height. If so this is a good indication that a proper quantum lifetime $\tau_{q, \text{MIRO}}$ has been chosen.
2. The nodal point between two integer values of ϵ_{ac} should exactly pass through a half-integer value of ϵ_{ac} , or to put it different the absolute plot of the cosine touches zero at integer (intrinsic) and half-integer values (fitting) of ϵ_{ac} . The fact that it touches zero at integer ϵ_{ac} is intrinsically due to the method of building up the interpolation function, which is subtracted afterwards to get rid of the background. The touching of zero at half-integer values of ϵ_{ac} is mainly influenced by the correct assumption for m^* .

The cosinusoidal approach is only valid for overlapping Landau levels, which may lead to deviations on the first (MIRO 1+, 1-) and weaker deviations on the second 2+ MIRO extrema. This is especially important for experiments on ZnO heterostructures since the high electron effective mass and Landé factor shift MIRO to higher magnetic fields. Therefore LL are already more separated.

Figure 7.3 shows the fitting results for the voltage pair with strongest MIRO signal (14)-(16). The different curves are scaled in a way that the MIRO 2+ feature has a fixed amplitude of ≈ 0.5 .

The upper panel shows a variation of the effective mass around the optimal value of $m^* = 0.327 m_e$ by 1.5%. This value is optimized in a way that the curve intersect with / touches zero at $\epsilon_{ac} = 2.5$. Also the different amplitudes of the 2+, 2- and 3+ feature are most similar in amplitude. None of the fits intersect with zero at $\epsilon_{ac} = 1.5$, which is attributed to the deviations from the cosinusoidal approach in the first MIRO extrema. Nevertheless, it should not be claimed here to provide a fitting of the effective mass with such high accuracy, but more to make it plausible that $m^* \approx 0.33 m_e$ is a plausible value. The tendencies which can be seen by varying m^* get even stronger if the value deviates more from the optimal one. An accuracy of 3% is reasonable to claim.

The bottom panel shows, that the variation of $\tau_{q, \text{MIRO}} = 3.25 \text{ ps}$ is more

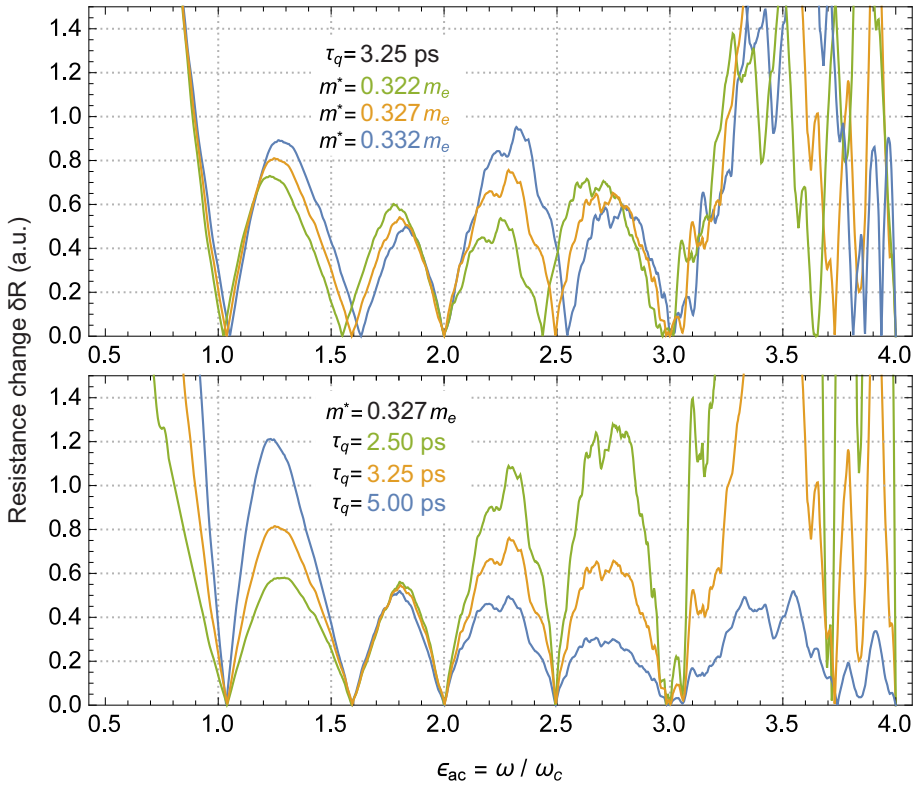


Figure 7.3: Analysis of the effective mass m^* (upper panel) and quantum lifetime $\tau_{q, \text{MIRO}}$ (bottom panel) in MIRO signals

sensitive to deviations towards shorter quantum lifetimes, than towards longer ones. If $\tau_{q, \text{MIRO}}$ is chosen to be too short, the MIRO dampening is assumed to be too high and therefore the term to compensate for MIRO dampening is also too high. MIRO amplitudes for consecutive extrema (e.g. 2+, 2-, 3+) continuously raise in amplitude and vice versa if $\tau_{q, \text{MIRO}}$ is chosen to be too long. The emphasis is not put on the exact value, but more on the claimed range.

Multiple voltage probes on one and the same sample show very comparable results and support the experimental finding for the quantum lifetime: $2.50 \text{ ps} < \tau_{q, \text{MIRO}} < 5.00 \text{ ps}$ and the electron effective mass: $0.322 m_e < m^* < 0.332 m_e$.

7.3 τ_q from MIPVO

The same technique that was used to extract the quantum lifetime of MIRO signals $\tau_{q, \text{MIRO}}$ is now applied to photovoltage signals to extract $\tau_{q, \text{MIPVO}}$. The only difference is, that the starting point is not the magnetoresistance but the photovoltage signal. Please refer to section 7.2 for detailed description of how the data is analyzed.

Figure 7.4 shows the fitting results for the voltage pair with the strongest MIPVO signal (21)-(20). The curves are scaled in a way that the MIPVO 2+ feature has a fixed amplitude of ≈ 4 . In comparison with the MIRO fitting in Figure 7.3 it is obvious that the MIPVO signal is stronger and features up to MIPVO 4- are observable.

The upper panel shows a variation of the effective mass around $m^* = 0.315 m_e$ by 1.6%. The fitting value is optimized to intersect with zero at $\epsilon_{ac} = 3.5$ and $\epsilon_{ac} = 4.5$. If the fitting value for the electron effective mass is chosen to be too small two things happen: First, the transition points between MIPVO extrema are shifted away from half-integer ϵ_{ac} towards smaller values and second the minima are smaller in amplitude compared to the maxima (e.g. 2+ compared to 2- or 3+ compared to 3-). If the electron effective mass is chosen to be too large the opposite happens.

The bottom panel illustrates, that the variation of $\tau_{q, \text{MIPVO}} = 3.25 \text{ ps}$ is

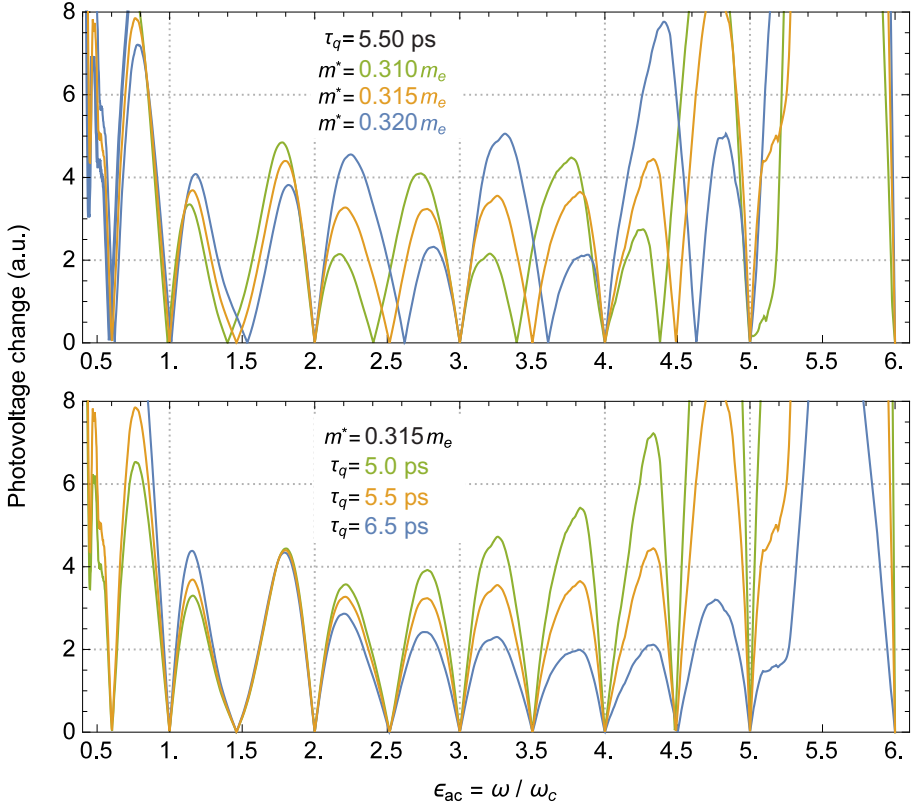


Figure 7.4: Analysis of the effective mass m^* (upper panel) and quantum lifetime $\tau_{q, \text{MIPVO}}$ (bottom panel) in MIPVO signals

more sensitive to deviations towards shorter quantum lifetimes, than towards longer ones. If $\tau_{q, \text{MIPVO}}$ is chosen to be too small, the MIPVO dampening is assumed to be too high and therefore the inverted correction is too large as well. MIPVO amplitudes for consecutive extrema (e.g. 3+, 3-, 4+, 4-) continuously rise in amplitude and vice versa if $\tau_{q, \text{MIPVO}}$ is chosen to be too long. The exact value is not as relevant, but rather the range of suitable $\tau_{q, \text{MIPVO}}$.

Multiple voltage probes on the same sample show very comparable results. $\tau_{q, \text{MIPVO}}$ lies in the range from 5.00 ps to 6.50 ps ($0.310 m_e < m^* < 0.320 m_e$). Interestingly the higher extracted quantum lifetime goes along with the occurrence of higher order MIPVO extrema, which indicate a correlation between the quantum lifetime and the occurrence of MIRO / MIPVO.

7.4 Comparison

This section compares the different electron quantum lifetimes τ_q and electron effective masses m^* obtained from the analysis of Shubnikov de-Haas oscillations (SdH) (section 7.1), microwave-induced resistance oscillations (MIRO) (section 7.2) and microwave-induced photovoltage oscillations (MIPVO) (section 7.3).

The following short paragraphs compare the signal formation of the 3 effects in order to demonstrate that the comparison of the quantum lifetimes with these 3 methods gives additional insight in the microscopic structure of the disorder of the sample. The signal formations are related to geometrical aspects of the sample, which are illustrated in Figure 7.5.

Shubnikov de-Haas oscillations

The measured resistance values of the Shubnikov de-Haas oscillations are strongly effected by the current path. Therefore the amplitudes and also the extraction of quantum lifetime $\tau_{q, \text{SdH}}$ is an integral quantity of the current path between the two voltage probes used in the 4 terminal measurement. This is indicated by a blue strip in Figure 7.5.

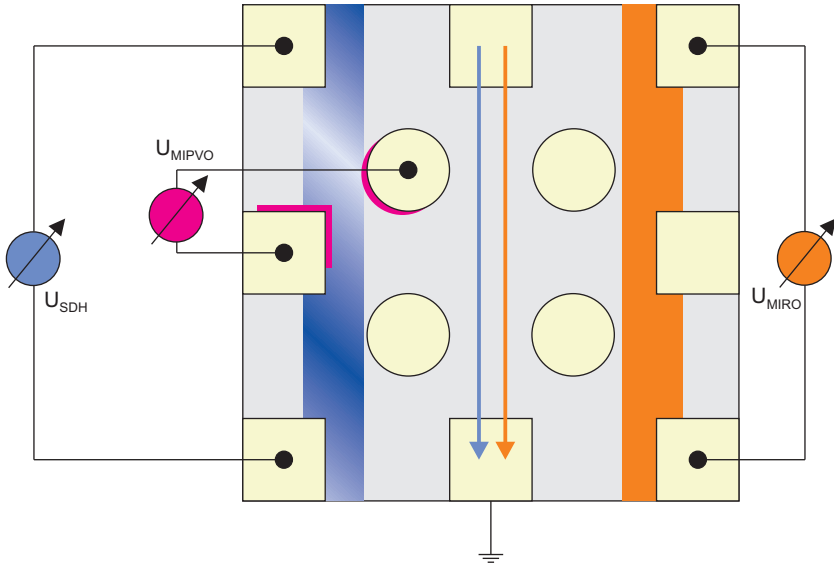


Figure 7.5: Spatial distribution of signal formation areas for different types of measurements: Shubnikov de-Haas oscillations (SdH) (blue), microwave-induced resistance oscillations (MIRO) (orange) and microwave-induced photovoltage oscillations (MIPVO) (magenta).

The amplitudes of Shubnikov de-Haas oscillations are not directly related to the electron density, as it can be seen from formula 1.12 on page 18. The same is true for the extracted quantum lifetimes $\tau_{q, \text{SdH}}$. Nevertheless, local changes in the carrier density affect the magnetic field position of Shubnikov de-Haas oscillations, which are summed up to the integral signal. The same is true for the electron mobility and disorder. Local variations in the Shubnikov de-Haas curves are summed up, and therefore the measured signal is affected by all local effects on the current path in the end (depicted as a color variation in Figure 7.5). This means that inhomogeneities in the carrier density and local disorder fluctuations can have a direct influence on the extracted quantum lifetime.

MIRO

Similar to SdH oscillations MIRO are also effected by the current path. But MIRO rely on the ratio of microwave photon energy to cyclotron energy $\epsilon_{ac} = \hbar\omega/\hbar\omega_c$, which is not dependent on electron density. Therefore the dampening of MIRO amplitudes is independent of local variations of the electron density. Different regions that contribute more or less (that have stronger or weaker MIRO signals) are summed up to the integral MIRO signal, which is used to extract the quantum lifetime $\tau_{q, \text{MIRO}}$.

MIPVO

Similar to MIRO, MIPVO are also independent of the charge carrier density. But the spatial area of signal formation is restricted to smaller areas near the contacts. The effective area of signal formation is much smaller compared to SdH and MIRO. Moreover, nearby metallic contact areas can have an influence on the disorder potential as they screen local fluctuations in the electron density.

Comparison

The following table compares the extracted values for the quantum lifetimes τ_q and electron effective masses m^* obtained from the analysis of SdH, MIRO and MIPVO:

	Shubnikov de-Haas	MIRO	MIPVO
$\tau_q(ps)$	0.29	3.25 (+1.75 -0.75)	5.50 (+1.00 -0.50)
$m^* (m_e)$	n.a.	0.327 (\pm 0.005)	0.315 (\pm 0.005)

The SdH, MIRO and MIPVO amplitudes are all related differently to the charge carrier density and spatial signal formation. Therefore the interpretation of extracted quantum lifetimes is complementary and provides insight in the electronic microstructure.

The fact that MIPVO experiments reveal the highest values for the quantum lifetime: $\tau_{q, \text{MIPVO}} > \tau_{q, \text{MIRO}} > \tau_{q, \text{SdH}}$, suggests itself that the quantum lifetime is mainly dominated by long-range effects and electron density fluctuations. In order to proof this indication further measurements with specialized geometries are necessary. For instance one could think about SdH experiments with voltage probes aligned very closely to each other.

It is up to future experiments to further develop a quantitative understanding of the microstructure by comparing quantum lifetimes from SdH, MIRO and MIPVO. Further control of geometric parameters (size, shape and position of contacts and the 2DES) may help figuring out length scales that describe the disorder potential. Nevertheless these experiments will be challenging because the geometry of the contacts has a major influence on the distribution of the microwave field nearby.

Chapter 8

Summary

8.1 English

This thesis covers the influence of microwave radiation on the two-dimensional electron gas in ZnO heterostructures. We investigated samples with different electron densities and found microwave-induced resistance oscillations (MIRO) on samples with densities higher than $3.9 \cdot 10^{11} \text{ cm}^{-2}$. This is the first observation of MIRO in an oxidic system and the third condensed matter system that shows MIRO at all. Moreover we also found microwave-induced oscillations in the photovoltage and photocurrent signals. The frequency dependence as well as power and temperature dependence were investigated in detail. They are found to be similar to MIRO in GaAs and SiGe systems.

A detailed analysis of the experimental results from Shubnikov de-Haas oscillations, microwave-induced resistance oscillations and photovoltage signals provides 3 different approaches to extract the effective mass and the quantum lifetime. Very high values for the quantum lifetime (higher than $\tau_{q, \text{MIPVO}} = 5 \text{ ps}$) were reported and underlie the low disorder level in these ZnO heterostructures. The quantum lifetime is found to be very different with the different techniques used. We assume that this is due to the spatial sensitivity of the

different measurement techniques. Hence, they can be used together as a kind of microscope to study disorder in two-dimensional systems on different length scales.

Up to now it is still unclear what are the key sample parameters that determine the strength of MIRO signals. A detailed analysis of the MIRO signal strength as a function of electron density, mobility and quantum lifetime may help finding out the missing material parameter in the future. Moreover the polarization dependency of the MIRO signal strength will be interesting to study, because spin transitions can be induced. Therefore ZnO is especially interesting because the Zeeman and cyclotron energy are comparable. Experiments in a quasi-optical setup may reveal spin-dependent effects and spin selection rules for MIRO in ZnO.

8.2 German

In dieser Arbeit wird der Einfluss von Mikrowellenstrahlung auf zweidimensionale Elektronensysteme in ZnO Heterostrukturen untersucht. Dabei haben wir Proben mit verschiedenen Elektronendichten untersucht und Mikrowellen induzierte Widerstandoszillationen (MIRO) an Proben mit Dichten höher als $3.9 \cdot 10^{11} \text{ cm}^{-2}$ gefunden. Dieser Effekte konnte das erste Mal in einem oxidischen System und überhaupt das dritte Mal an einem Festkörpersystem gefunden werden. Darüber hinaus konnten Mikrowellen induzierte Oszillationen in den Photospannungs- und Photostromsignalen gemessen werden. Das Frequenzverhalten sowie die Leistungs- und Temperaturabhängigkeit wurden im Detail untersucht. Sie zeigen ähnliches Verhalten wie aus GaAs und SiGe Systemen bekannt.

Eine detaillierte Auswertung der experimentellen Ergebnisse von Shubnikov de-Haas Oszillationen, Mikrowellen induzierten Widerstandoszillationen und Photospannungssignalen stellt drei Zugänge dar die effektive Masse und die Quantenlebensdauer zu extrahieren. Hohe Werte für die Quantenlebensdauer von über $\tau_{q, \text{MIPVO}} = 5 \text{ ps}$ werden berichtet und unterstreichen die herausragend niedrige Unordnung in diesen ZnO Heterostrukturen. Für die Quantenlebensdauer ergeben sich dabei sehr verschiedene Werte für die hier verwendete

ten Untersuchungsmethoden. Es wird angenommen, dass dies auf die unterschiedliche räumlichen Sensitivität der verschiedenen Messmethoden zurückgeht. Zusammengenommen können diese Methoden als eine Art Mikroskop eingesetzt werden um die Unordnung in zweidimensionalen Systemen auf unterschiedlichen Längenskalen zu untersuchen.

Bis heute ist unklar welche Materialparameter für die MIRO Signalstärke entscheidend sind. Eine detaillierte Analyse der MIRO Signalstärke als Funktion der Elektronendichte, Mobilität und Quantenlebensdauer kann zukünftig helfen die entscheidenden Materialparameter aufzudecken. Darüber hinaus wird es interessant sein die Polarisationsabhängigkeit der MIRO Signalstärke zu untersuchen um Spinübergänge induzieren zu können. Dabei bietet sich ZnO an weil die Zeeman- und Zyklotronenergie vergleichbar sind und damit durch Magnetfelder in der Ebene Kreuzungen zwischen verschiedenen Landauniveaus hervorgerufen werden können. Experimente in einem quasi-optischen Aufbau könnten spinabhängige Effekte und Spinauswahlregeln für MIRO in ZnO zu Tage bringen.

Part III

Appendix

Chapter 9

Cyclotron resonance absorption

This section deals with the observation of cyclotron resonance absorption (CRA) in transport, which shows up in low carrier density samples only where MIRO are absent. CRA manifests itself as an increase in the magnetoresistance at a magnetic field, which corresponds to $\omega = \omega_c$, as shown in Figure 9.1 (inset). In contrast to MIRO, CRA do not lead to features in resistance at higher harmonics of ω_c , a selection rule prevents transitions with $\Delta N \neq 1$ (see equation 3.1 on page 30).

From a theoretical perspective one can think of a microwave photon exciting an electron in a occupied LL n to a higher (partially) unoccupied LL $n + 1$. The excitation relaxes and therefore heats up the electronic system which leads to an increase in resistivity.

As shown in Figure 9.1 the peak position (in magnetic field) of the CRA moves linearly with the microwave frequency and contains the effective mass m^* of the ZnO host as a material. An average effective mass (red arrow) of $m_{\text{CRA}}^* = 0.30 m_e$ is found when taking the mean of all values extracted at different frequencies (red dots).

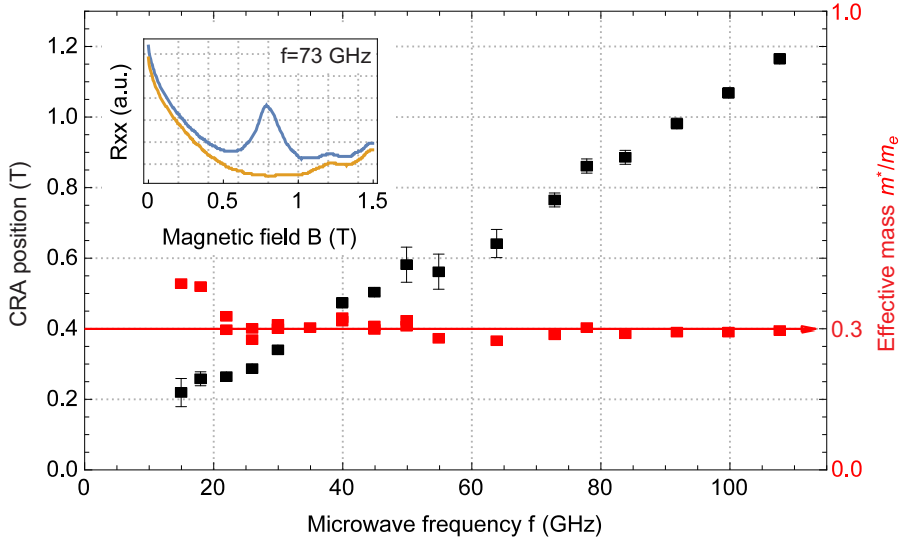


Figure 9.1: Magnetic field position of the cyclotron resonance peak in the magnetoresistance as a function of the microwave frequency. Shown in red is the calculated effective mass. The average for all frequencies yields $m^* = 0.30 m_e$. An empirical error bar was added to data points with very low amplitude (due to low microwave powers, see next chapter). The inset shows an example of two magnetoresistance curves in the absence and presence of microwave radiation ($f = 73$ GHz).

We note that the line width of CRA is not only determined by the quantum lifetime τ_q , but can be broadened by orders of magnitude under the influence of saturation effects [86] referred to as radiative decay [87].

Chapter 10

Electrical transport measurement setup

This chapter is intended to be a practical guide for electrical measurements. Within the framework of this thesis a cryosystem including electrical setup was moved and rebuild. The improvements are documented here. It also includes notes on measuring ultra-low resistances (e.g. superconductors) as it was done for this thesis, but not covered in the main text.

10.1 Avoiding ground loops

Ground loops occur whenever there is a closed electric circuit on ground potential. They pick up magnetic stray fields and can therefore raise the noise floor in electrical measurements substantially. The general idea to avoid ground loops is to provide the mass of the measurement system in a star like configuration with the cryostat at the center. Ideally the cryostat itself is connected to a special measurement mass, which is only used for scientific experiments and not for other purposes (e.g. building services).

For every instrument that is connected to the measurement setup, it needs to be checked whether the output and input terminals are connected to the cryostat ground and whether they have a connection to the grounding of the instruments power supply. If so this would close the ground loop and is therefore unwanted. In our case this is true for more than 50% of the instruments.

With the use of isolation transformers measurement devices can be galvanically isolated from its mass and hence potential ground loops are interrupted. The isolation transformers themselves are sources for electric and magnetic stray fields and should be placed far away from the experiment or in a shielded environment.

Special attention has to be paid to the power supply of magnet systems. In these devices very high currents (above 100 A) are generated and for security reasons a connection to ground is necessary. Oxford Instruments advises to make sure not to overcome a potential difference of 40 V between the mass of the power supply and the cryostat [88]. This can be ensured by a diode circuit that separates the potential of the power supply and the cryostat up to 35V. One has to rely on home build circuits, because there is no commercial solution available from Oxford Instruments.

The same care has to be taken on the signal readout from the instruments. In our case we mainly use IEC-625-Bus (GPIB) technology which is transmitted via a shielded cable. This shielding interconnects the ground potential of different instruments and causes ground loops. We use special GPIB optocouplers from National instruments to decouple the instrument setup. A similar argument holds for instruments that are read out by RS232 (serial port). Wiesemann & Theis GmbH is offering cable-integrated optocoupler for serial ports, which are convenient to use.

In order to measure voltage or current signals with the help of lock-in amplifiers, they need to be connected to a frequency reference signal of the AC source (sync signal). The signal is usually transmitted via BNC cables. We use special home built optocouplers to galvanically isolate the lock-in amplifiers from each other to avoid a ground loops.

A very common task is to measure a potential difference (A–B) with two BNC cables. Here the shielding of the cables leads to a ground loop. Experiments

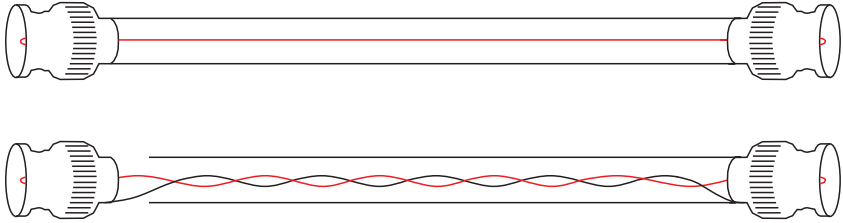


Figure 10.1: Schematic of conventional (top) and specialized (bottom) BNC cable with electromagnetic shielding in sack geometry to enhance series-mode interference suppression. The signal line is colored in red.

with a defined interruption in the shielding show that in most cases the benefit of avoiding a ground loop has to be paid with higher stray pick-up, that is caused by interrupting the shielding. Therefore, it is not advisable to interrupt the shielding when measuring in A–B mode. It is plausible, that having a ground loop on the cable shielding is not as bad as having stray signals. In our experimental setup we twist the pair of BNC cables and use specially shielded BNC cables to further improve signal quality (see section 10.2).

Finally one ends up with an electrical setup and a star-like distributed mass. This is also convenient because it can easily be modified into a floating setup, which is necessary when measuring ultra low resistances (see section 10.3)

10.2 Signal cables

Lots of measurement instruments for electrical characterization use BNC connectors. BNC (Bayonet Neill Concelman) cables are developed to have a broad field of application. Usually they are used when either high frequencies or special demands concerning electromagnetic shielding are desired. Especially for high frequency applications there are multiple configurations with defined characteristic impedances (like 50 or 70 Ω).

In our case these measurements are carried out with the help of lock-in amplifiers to reduce the noise level. We use frequencies, such as 13.333 Hz

or 27,777 Hz, which are sufficiently low enough to probe the DC behavior of the system and incommensurate to power line frequencies, like the 50 Hz line frequency or 60 Hz, which is very often emitted by vacuum pumps. These low frequencies do not require the high frequency properties that come with conventional BNC cables, but are intended to use the good shielding qualities.

In order to further improve stray pickup of the signal cables we use a special geometry, which was developed for high fidelity (HiFi) audio equipment. Figure 10.1 shows a schematic of a conventional and a specialized BNC cable with series-mode interference suppression. The shielding is only connected to one end of the BNC cable (which should point to the cryostat mass). This is called a sack geometry. Additionally, the shielding is transferred from one end to another as a twisted lead with the signal line (red). Therefore magnetic stray pick-up in between the shielding and the signal cable is strongly suppressed and the overall inductance, which is directly proportional to electrostatic stray pick-up is minimized. As a drawback the cable is no more suitable for high frequency applications.

We use the commercially available HMS Duetto MK III cable with BNC connectors to connect the measurement instruments with the sample rod. Their specifications claim a resistance of $R = 71.4 \text{ m}\Omega/\text{m}$, an inductance of $L = 0.45 \text{ }\mu\text{H}/\text{m}$ and capacity of $C = 65 \text{ pF}/\text{m}$.

10.3 Common-mode rejection ratio (CMRR)

Instruments that measure a voltage difference do this by using an operational amplifier (or multiple if the circuit is more complex). Independent of the details of the differential amplifier, there are 4 defined electric potentials: With respect to ground potential, there is a potential difference (V_s), which serves as a power supply for the operational amplifier and the two measurement potentials (A and B). This is depicted in Figure 10.2 (top). For an ideal differential amplifier only the voltage difference (A-B) is amplified. Real amplifiers however are influenced by the voltage difference to ground potential. This is quantified by the so called common mode rejection ratio (CMRR) which gives the logarithmic ratio of the amplification of the voltage difference A_D with respect to the amplification to

the voltage difference to ground potential (the common mode) A_{CM} :

$$CMRR = 20 \log \frac{A_D}{A_{CM}} \quad (10.1)$$

Typical values for CMRR are between 80 and 100 dB.

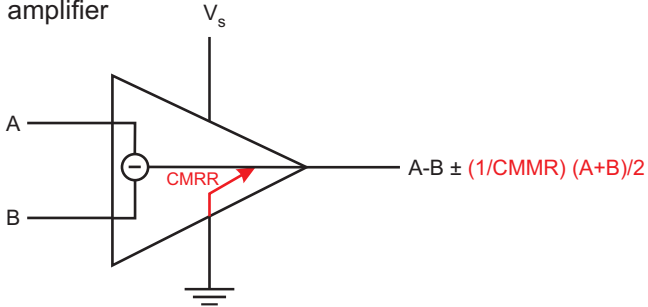
In a typical setup to measure electrical resistance a known current is passed through the sample while the voltage drop across the sample is measured, as shown in Figure 10.2 (middle). For highly conductive samples usually the contact resistances are bigger than the sample resistances one wants to measure. Or to express with potentials: the potential drop to be measured is much smaller than the source-drain potential drop. This leads to a high common mode which can significantly change the results of the measurement. Especially when you think about recording temperature dependent resistance data, not only the actual resistance of the sample but also the contact resistances can change abruptly. One also needs to measure the common mode, which is nothing else than recording the two-terminal drain resistance, in order to verify measured resistance changes as changes to the resistance within the sample.

Another way to overcome the problem with common mode issues is shown in Figure 10.2 (bottom). Here the sample is grounded with an additional voltage probe in the vicinity of the probes that are used to measure the actual resistance. The drain contact is floating which itself needs a floating setup in order to pass a floating current (please refer to section 10.1). Therefore the common mode created by the drain potential drop can be avoided. This minimizes the common-mode influence on the measured signal.

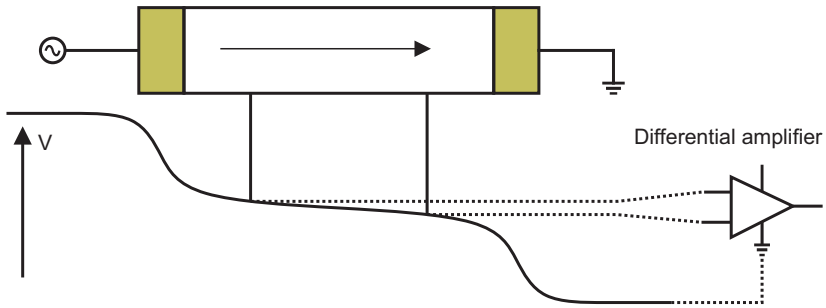
10.4 Asymmetric input resistances

Asymmetric contact resistances on the potential probes can have a huge influence on the measurement of resistances dependent on the common mode potential of the system. An equivalent circuit for a simple measurement setup is shown in Figure 10.3 (top). Overall in this scheme there are 3 possible ways for the current I to flow from source to drain: Either through the sample (sample resistance r_s and drain / common mode resistance r_{cm}) or through any of

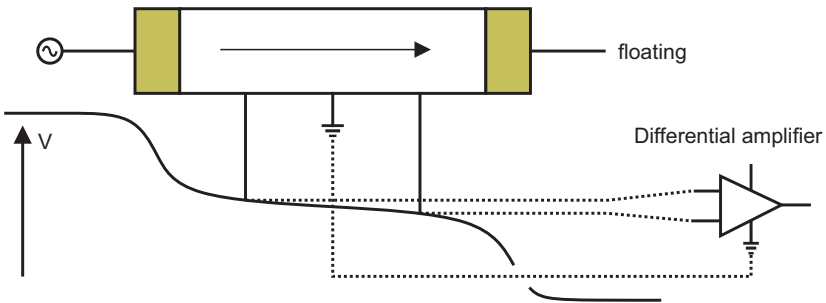
Differential amplifier



Grounded drain



Floating drain



the voltage probes. Since the input resistances of lock-in amplifiers are very high (Stanford SRS830 used in our experiments have an input resistance of $r_{in} = 10\text{ M}\Omega$), the main current flows through the sample and drain contact. (A source contact has no influence on the measured resistance and is therefore left out in this consideration.)

Currents through the different paths are calculated and used to calculate the potential at A and B. The measured resistance $(A-B)/I$ is calculated and compared to the actual value. The error (deviation of measured to actual resistance) is plotted against the ratio of common mode resistance to signal (actual sample resistance) in Figure 10.3 for different asymmetric contact resistances. As an example a sample resistance of $r_s = 10\ \Omega$ and a contact resistance of $r_{c1} = 10\ \Omega$ is chosen. The second contact resistance r_{c2} is varied between 10 and $10^6\ \Omega$.

An additional effect comes into play if one considers phase variations of the AC signal due to asymmetric contact resistances. If a lock-in technique is used to measure resistances the asymmetric (contact) resistances shift the phase of the signal. Usually this effect is very small (below 0.1%), but gets more important the higher the frequency is. As a rule of thumb one is safe (error below 1%) as long as the asymmetry of the contacts times the measurement frequency is below 10^6 . In our case, the error due to phase shifts was smaller than the error due to parallel conductivity.

Overall, it is advisable to choose the contact with the lowest possible resistance as a drain contact and to choose the voltage probes with similar contact resistances as pairs (A and B).

Figure 10.2 (*preceding page*): Top: Schematic of a differential amplifier and the common mode rejection ratio (CMRR). Middle and bottom: Schematics of measurement scheme with grounded and floating drain. Also the potential profile across the sample is shown in a diagram. The potential drops over the contact areas (golden) usually dominate for highly conductive samples.

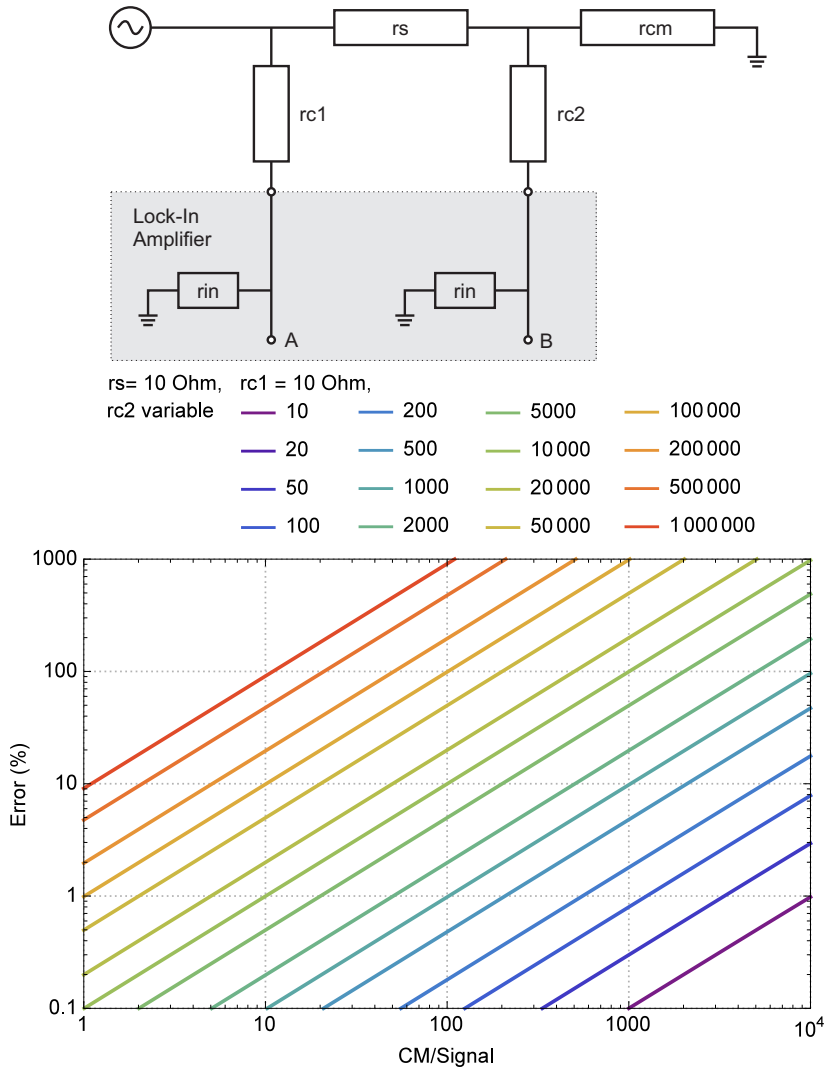


Figure 10.3: Influence of asymmetric input resistances on the error of the measured resistance

Bibliography

- [1] J. H. Davies, *The physics of low-dimensional semiconductors: An introduction*. Cambridge University Press, 1998.
- [2] S. Datta, *Electronic transport in mesoscopic systems*. Cambridge University Press, 1995.
- [3] S. Hunklinger, *Festkörperphysik*. Oldenburg Verlag, 2007.
- [4] P. Drude, “On the electron theory of metals,” *Annalen Der Physik*, vol. 1, no. 3, pp. 566–613, 1900.
- [5] S. Das Sarma and F. Stern, “Single-particle relaxation time versus scattering time in an impure electron gas,” *Physical Review B*, vol. 32, no. 12, pp. 8442–8444, 1985.
- [6] J. Nübler, *Density dependence of the $\nu = 5/2$ Fractional Quantum Hall Effect - Compressibility of a Two-dimensional Electron System under Microwave Radiation*. PhD thesis, 2012.
- [7] P. T. Coleridge, R. Stoner, and R. Fletcher, “Low-field transport coefficients in GaAs/AlGaAs heterostructures,” *Physical Review B*, vol. 39, no. 2, pp. 1120–1124, 1989.

- [8] P. T. Coleridge, “Small-angle scattering in two-dimensional electron gases,” *Physical Review B*, vol. 44, no. 8, pp. 3793–3801, 1991.
- [9] V. Mosser, D. Weiss, K. von Klitzing, K. Ploog, and G. Weimann, “Density of states of GaAs/AlGaAs heterostructures deduced from temperature-dependent magneto capacitance measurements,” *Solid State Communications*, vol. 58, no. 1, pp. 5–7, 1986.
- [10] T. P. Smith, B. B. Goldberg, P. J. Stiles, and M. Heiblum, “Direct measurement of the density of states of a two-dimensional electron-gas,” *Physical Review B*, vol. 32, no. 4, pp. 2696–2699, 1985.
- [11] J. P. Eisenstein, H. L. Stormer, V. Narayanamurti, A. Y. Cho, A. C. Gossard, and C. W. Tu, “Density of states and de Haas - van Alphen effect in two-dimensional electron-systems,” *Physical Review Letters*, vol. 55, no. 8, pp. 875–878, 1985.
- [12] R. C. Ashoori and R. H. Silsbee, “The landau-level density of states as a function of fermi energy in the 2-dimensional electron-gas,” *Solid State Communications*, vol. 81, no. 10, pp. 821–825, 1992.
- [13] A. Potts, R. Shepherd, W. G. Herrenden-Harker, M. Elliott, C. L. Jones, A. Usher, G. A. Jones, D. A. Ritchie, E. H. Linfield, and G. M., “Magnetization studies of Landau level broadening in two-dimensional electron systems,” *Journal of Physics-Condensed Matter*, vol. 8, no. 28, pp. 5189–5207, 1996.
- [14] K. von Klitzing, G. Dorda, and M. Pepper, “New method for high-accuracy determination of the fine-structure constant based on quantized hall resistance,” *Physical Review Letters*, vol. 45, no. 6, pp. 494–497, 1980.
- [15] J. Weis and K. von Klitzing, “Metrology and microscopic picture of the integer quantum hall effect,” *Philosophical Transactions of the Royal Soci-*

-
- ety a-Mathematical Physical and Engineering Sciences*, vol. 369, no. 1953, pp. 3954–3974, 2011.
- [16] R. Landauer, “Electrical transport in open and closed systems,” *Physical Review B*, vol. 68, no. 2-3, pp. 217–228, 1987.
- [17] M. Buttiker, “Absence of backscattering in the quantum Hall-effect in multi probe conductors,” *Physical Review B*, vol. 38, no. 14, pp. 9375–9389, 1988.
- [18] D. B. Chklovskii, B. I. Shklovskii, and L. I. Glazman, “Electrostatics of edge channels,” *Physical Review B*, vol. 46, no. 7, pp. 4026–4034, 1992.
- [19] D. B. Chklovskii, K. A. Matveev, and B. I. Shklovskii, “Ballistic conductance of interacting electrons in the quantum Hall regime,” *Physical Review B*, vol. 47, no. 19, pp. 12605–12617, 1993.
- [20] D. C. Tsui, H. L. Stormer, and A. C. Gossard, “Two-dimensional magneto transport in the extreme quantum limit,” *Physical Review Letters*, vol. 48, no. 22, pp. 1559–1562, 1982.
- [21] J. K. Jain, *Composite fermions*. Cambridge University Press, 2007.
- [22] R. L. Willett, “The quantum hall effect at $5/2$ filling factor,” *Reports on Progress in Physics*, vol. 76, no. 7, 2013.
- [23] G. Moore and N. Read, “Nonabelions in the fractional quantum Hall-effect,” *Nuclear Physics B*, vol. 360, no. 2-3, pp. 362–396, 1991.
- [24] J. Falson, *Transport phenomena and correlation effects in MgZnO/ZnO interface confined high mobility two-dimensional electron systems*. PhD thesis, 2015.
- [25] D. G. Schlom and L. N. Pfeiffer, “Oxide electronics: Upward mobility rocks!,” *Nature Materials*, vol. 9, no. 11, pp. 881–883, 2010.

- [26] H. Y. Hwang, Y. Iwasa, M. Kawasaki, B. Keimer, N. Nagaosa, and Y. Tokura, “Emergent phenomena at oxide interfaces,” *Nat Mater*, vol. 11, no. 2, pp. 103–113, 2012.
- [27] A. Shunsuke, N. Ken, Y. Hiroyuki, T. Atsushi, O. Akira, and K. Masashi, “Preparation of an epitaxy-ready surface of a ZnO(0001) substrate,” *Applied Physics Express*, vol. 4, no. 3, p. 035701, 2011.
- [28] Y. Kozuka, A. Tsukazaki, and M. Kawasaki, “Challenges and opportunities of ZnO-related single crystalline heterostructures,” *Applied Physics Reviews*, vol. 1, no. 1, p. 011303, 2014.
- [29] J. Falson, D. Maryenko, Y. Kozuka, A. Tsukazaki, and M. Kawasaki, “Magnesium doping controlled density and mobility of two-dimensional electron gas in MgZnO/ZnO heterostructures,” *Applied Physics Express*, vol. 4, no. 9, p. 091101, 2011.
- [30] M. A. Zudov, R. R. Du, J. A. Simmons, and J. L. Reno, “Shubnikov-de haas-like oscillations in millimeterwave photoconductivity in a high-mobility two-dimensional electron gas,” *Physical Review B*, vol. 64, no. 20, p. 201311, 2001.
- [31] P. D. Ye, L. W. Engel, D. C. Tsui, J. A. Simmons, J. R. Wendt, G. A. Vawter, and J. L. Reno, “Giant microwave photoresistance of two-dimensional electron gas,” *Applied Physics Letters*, vol. 79, no. 14, pp. 2193–2195, 2001.
- [32] R. G. Mani, J. H. Smet, K. von Klitzing, V. Narayanamurti, W. B. Johnson, and V. Umansky, “Zero-resistance states induced by electromagnetic-wave excitation in GaAs/AlGaAs heterostructures,” *Nature*, vol. 420, no. 6916, pp. 646–650, 2002.

- [33] R. Fitzgerald, “Microwaves induce vanishing resistance in two-dimensional electron systems,” *Physics Today*, vol. 56, no. 4, pp. 24–27, 2003.
- [34] A. C. Durst and S. M. Girvin, “Cooking a two-dimensional electron gas with microwaves,” *Science*, vol. 304, no. 5678, pp. 1752–1753, 2004.
- [35] D. Konstantinov and K. Kono, “Novel radiation-induced magnetoresistance oscillations in a nondegenerate two-dimensional electron system on liquid helium,” *Physical Review Letters*, vol. 103, no. 26, p. 266808, 2009.
- [36] D. Konstantinov and K. Kono, “Photon-induced vanishing of magnetoconductance in 2d electrons on liquid helium,” *Physical Review Letters*, vol. 105, no. 22, p. 226801, 2010.
- [37] M. A. Zudov, O. A. Mironov, Q. A. Ebner, P. D. Martin, Q. Shi, and D. R. Leadley, “Observation of microwave-induced resistance oscillations in a high-mobility two-dimensional hole gas in a strained Ge/SiGe quantum well,” *Physical Review B*, vol. 89, no. 12, p. 125401, 2014.
- [38] V. I. Ryzhii *Sov. Phys. Solid State*, vol. 11, p. 2078, 1970.
- [39] V. I. Ryzhii, R. A. Suris, and B. S. Shchamkhalova *Sov. Phys. Semicond.*, vol. 20, p. 1299, 1986.
- [40] I. A. Dmitriev, A. D. Mirlin, D. G. Polyakov, and M. A. Zudov, “Nonequilibrium phenomena in high landau levels,” *Reviews of Modern Physics*, vol. 84, no. 4, pp. 1709–1763, 2012.
- [41] A. C. Durst, S. Sachdev, N. Read, and S. M. Girvin, “Radiation-induced magnetoresistance oscillations in a 2d electron gas,” *Physical Review Letters*, vol. 91, no. 8, p. 086803, 2003.

- [42] X. L. Lei and S. Y. Liu, “Radiation-induced magnetoresistance oscillation in a two-dimensional electron gas in Faraday geometry,” *Physical Review Letters*, vol. 91, no. 22, p. 226805, 2003.
- [43] V. Ryzhii and R. Suris, “Nonlinear effects in microwave photoconductivity of two-dimensional electron systems,” *Journal of Physics Condensed Matter*, vol. 15, no. 40, pp. 6855–6869, 2003.
- [44] M. G. Vavilov and I. L. Aleiner, “Magnetotransport in a two-dimensional electron gas at large filling factors,” *Physical Review B*, vol. 69, no. 3, p. 035303, 2004.
- [45] S. I. Dorozhkin, “Giant magnetoresistance oscillations caused by cyclotron resonance harmonics,” *JETP Letters*, vol. 77, no. 10, pp. 577–581, 2003.
- [46] I. A. Dmitriev, A. D. Mirlin, and D. G. Polyakov, “Cyclotron-resonance harmonics in the ac response of a 2d electron gas with smooth disorder,” *Physical Review Letters*, vol. 91, no. 22, p. 226802, 2003.
- [47] I. A. Dmitriev, M. G. Vavilov, I. L. Aleiner, A. D. Mirlin, and D. G. Polyakov, “Theory of microwave-induced oscillations in the magnetoconductivity of a two-dimensional electron gas,” *Physical Review B*, vol. 71, no. 11, p. 115316, 2005.
- [48] I. A. Dmitriev, A. D. Mirlin, and D. G. Polyakov, “Oscillatory ac conductivity and photoconductivity of a two-dimensional electron gas: Quasiclassical transport beyond the boltzmann equation,” *Physical Review B*, vol. 70, no. 16, p. 165305, 2004.
- [49] I. A. Dmitriev, A. D. Mirlin, and D. G. Polyakov, “Microwave photoconductivity of a two-dimensional electron gas: Mechanisms and their interplay at high radiation power,” *Physical Review B*, vol. 75, no. 24, p. 245320, 2007. PRB.

- [50] S. A. Mikhailov, “Theory of microwave-induced zero-resistance states in two-dimensional electron systems,” *Physical Review B - Condensed Matter and Materials Physics*, vol. 83, no. 15, 2011.
- [51] O. E. Raichev, “Microwave-induced magnetoresistance of two-dimensional electrons interacting with acoustic phonons,” *Physical Review B*, vol. 81, no. 16, 2010.
- [52] V. Ryzhii, “Microwave photoconductivity in two-dimensional electron systems due to photon-assisted interaction of electrons with leaky interface phonons,” *Physical Review B - Condensed Matter and Materials Physics*, vol. 68, no. 19, pp. 1934021–1934024, 2003.
- [53] V. Ryzhii and V. Vyurkov, “Absolute negative conductivity in two-dimensional electron systems associated with acoustic scattering stimulated by microwave radiation,” *Physical Review B - Condensed Matter and Materials Physics*, vol. 68, no. 16, pp. 1654061–1654068, 2003.
- [54] A. Koulakov and M. Raikh, “Classical model for the negative dc conductivity of ac-driven two-dimensional electrons near the cyclotron resonance,” *Physical Review B*, vol. 68, no. 11, p. 115324, 2003.
- [55] P. Rivera and P. Schulz, “Radiation-induced zero-resistance states: Possible dressed electronic structure effects,” *Physical Review B*, vol. 70, no. 7, p. 075314, 2004.
- [56] J. Shi and X. Xie, “Radiation-induced zero-resistance state and the photon-assisted transport,” *Physical Review Letters*, vol. 91, no. 8, p. 086801, 2003.
- [57] J. Inarrea and G. Platero, “Theoretical approach to microwave-radiation-induced zero-resistance states in 2D electron systems,” *Physical Review Letters*, vol. 94, no. 1, 2005.

- [58] A. D. Chepelianskii and D. L. Shepelyansky, “Microwave stabilization of edge transport and zero-resistance states,” *Physical Review B - Condensed Matter and Materials Physics*, vol. 80, no. 24, 2009.
- [59] A. D. Chepelianskii, A. S. Pikovsky, and D. L. Shepelyansky, “Synchronization, zero-resistance states and rotating wigner crystal,” *European Physical Journal B*, vol. 60, no. 2, pp. 225–229, 2007.
- [60] C. L. Yang, M. A. Zudov, T. A. Knuuttila, R. R. Du, L. N. Pfeiffer, and K. W. West, “Observation of microwave-induced zero-conductance state in corbino rings of a two-dimensional electron system,” *Physical Review Letters*, vol. 91, no. 9, p. 096803, 2003.
- [61] R. Willett, L. Pfeiffer, and K. West, “Evidence for current-flow anomalies in the irradiated 2d electron system at small magnetic fields,” *Physical Review Letters*, vol. 93, no. 2, p. 026804, 2004.
- [62] A. Wirthmann, B. D. McCombe, D. Heitmann, S. Holland, K.-J. Friedland, and C.-M. Hu, “Far-infrared-induced magnetoresistance oscillations in gaas/algaas-based two-dimensional electron systems,” *Physical Review B*, vol. 76, no. 19, p. 195315, 2007.
- [63] S. A. Studenikin, A. S. Sachrajda, J. A. Gupta, Z. R. Wasilewski, O. M. Fedorych, M. Byszewski, D. K. Maude, M. Potemski, M. Hilke, K. W. West, and L. N. Pfeiffer, “Frequency quenching of microwave-induced resistance oscillations in a high-mobility two-dimensional electron gas,” *Physical Review B*, vol. 76, no. 16, p. 165321, 2007.
- [64] M. A. Zudov, “Period and phase of microwave-induced resistance oscillations and zero-resistance states in two-dimensional electron systems,” *Physical Review B*, vol. 69, no. 4, p. 041304, 2004.

- [65] M. A. Zudov, R. R. Du, L. N. Pfeiffer, and K. W. West, “Evidence for a new dissipationless effect in 2d electronic transport,” *Physical Review Letters*, vol. 90, no. 4, p. 046807, 2003.
- [66] A. T. Hatke, M. A. Zudov, L. N. Pfeiffer, and K. W. West, “Giant microwave photoresistivity in high-mobility quantum hall systems,” *Physical Review B*, vol. 83, no. 12, p. 121301, 2011.
- [67] A. T. Hatke, M. Khodas, M. A. Zudov, L. N. Pfeiffer, and K. W. West, “Multiphoton microwave photoresistance in a high-mobility two-dimensional electron gas,” *Physical Review B*, vol. 84, no. 24, p. 241302, 2011.
- [68] A. T. Hatke, M. A. Zudov, L. N. Pfeiffer, and K. W. West, “Role of electron-electron interactions in nonlinear transport in two-dimensional electron systems,” *Physical Review B*, vol. 79, no. 16, p. 161308, 2009.
- [69] S. A. Studenikin, M. Potemski, A. Sachrajda, M. Hilke, L. N. Pfeiffer, and K. W. West, “Microwave-induced resistance oscillations on a high-mobility two-dimensional electron gas: Exact waveform, absorption, reflection and temperature damping,” *Physical Review B*, vol. 71, no. 24, p. 245313, 2005.
- [70] A. T. Hatke, M. A. Zudov, L. N. Pfeiffer, and K. W. West, “Temperature dependence of microwave photoresistance in 2d electron systems,” *Physical Review Letters*, vol. 102, no. 6, p. 066804, 2009.
- [71] C. L. Yang, R. R. Du, L. N. Pfeiffer, and K. W. West, “Influence of a parallel magnetic field on the microwave photoconductivity in a high-mobility two-dimensional electron system,” *Physical Review B*, vol. 74, no. 4, p. 045315, 2006.
- [72] A. Bogan, A. T. Hatke, S. A. Studenikin, A. Sachrajda, M. A. Zudov, L. N. Pfeiffer, and K. W. West, “Microwave-induced resistance oscillations

- in tilted magnetic fields,” *Physical Review B*, vol. 86, no. 23, p. 235305, 2012.
- [73] R. G. Mani, “Radiation-induced oscillatory magnetoresistance in a tilted magnetic field in GaAs/AlGaAs devices,” *Physical Review B*, vol. 72, no. 7, p. 075327, 2005.
- [74] A. A. Bykov, A. K. Bakarov, D. R. Islamov, and A. I. Toropov, “Giant magnetoresistance oscillations induced by microwave radiation and a zero-resistance state in a 2d electron system with a moderate mobility,” *JETP Letters*, vol. 84, no. 7, pp. 391–394, 2006.
- [75] A. T. Hatke, M. A. Zudov, J. D. Watson, M. J. Manfra, L. N. Pfeiffer, and K. W. West, “Evidence for effective mass reduction in GaAs/AlGaAs quantum wells,” *Physical Review B*, vol. 87, no. 16, p. 161307, 2013.
- [76] S. M. Sze, *Physics of Semiconductor Devices*. 1981.
- [77] A. V. Andreev, I. L. Aleiner, and A. J. Millis, “Dynamical symmetry breaking as the origin of the zero-dc-resistance state in an ac-driven system,” *Physical Review Letters*, vol. 91, no. 5, p. 056803, 2003.
- [78] S. I. Dorozhkin, L. Pfeiffer, K. West, K. von Klitzing, and J. H. Smet, “Random telegraph photosignals in a microwave-exposed two-dimensional electron system,” *Nature Physics*, vol. 7, no. 4, pp. 336–341, 2011.
- [79] S. I. Dorozhkin, I. V. Pechenezhskiy, L. N. Pfeiffer, K. W. West, V. Umansky, K. von Klitzing, and J. H. Smet, “Photocurrent and photovoltage oscillations in the two-dimensional electron system: Enhancement and suppression of built-in electric fields,” *Physical Review Letters*, vol. 102, no. 3, p. 036602, 2009.

- [80] I. A. Dmitriev, S. I. Dorozhkin, and A. D. Mirlin, “Theory of microwave-induced photocurrent and photovoltage magneto-oscillations in a spatially nonuniform two-dimensional electron gas,” *Physical Review B*, vol. 80, no. 12, p. 125418, 2009.
- [81] J. H. Smet, B. Gorshunov, C. Jiang, L. Pfeiffer, K. West, V. Umansky, M. Dressel, R. Meisels, F. Kuchar, and K. von Klitzing, “Circular-polarization-dependent study of the microwave photoconductivity in a two-dimensional electron system,” *Physical Review Letters*, vol. 95, no. 11, p. 116804, 2005.
- [82] S. A. Mikhailov and N. A. Savostianova, “Influence of contacts on the microwave response of a two-dimensional electron stripe,” *Physical Review B*, vol. 74, no. 4, p. 045325, 2006.
- [83] S. Wiedmann, G. M. Gusev, O. E. Raichev, A. K. Bakarov, and J. C. Portal, “Nonlinear transport phenomena in a two-subband system,” *Physical Review B*, vol. 84, no. 16, p. 165303, 2011.
- [84] R. G. Mani, A. N. Ramanayaka, and W. Wegscheider, “Observation of linear-polarization-sensitivity in the microwave-radiation-induced magnetoresistance oscillations,” *Physical Review B*, vol. 84, no. 8, p. 085308, 2011.
- [85] B. L. Altshuler, D. Khmel’nitzkii, A. I. Larkin, and P. A. Lee, “Magnetoresistance and Hall effect in a disordered two-dimensional electron gas,” *Physical Review B*, vol. 22, no. 11, pp. 5142–5153, 1980.
- [86] D. Heitman, M. Ziesmann, and L. L. Chang, “Cyclotron-resonance oscillations in InAs quantum wells,” *Physical Review B*, vol. 34, no. 10, pp. 7463–7466, 1986.

- [87] S. A. Mikhailov, “Microwave-induced magnetotransport phenomena in two-dimensional electron systems: Importance of electrodynamic effects,” *Physical Review B*, vol. 70, no. 16, p. 165311, 2004.
- [88] O. I. Superconductivity, “Operator’s handbook: Superconducting magnet system,” 2004.

Acknowledgements

Without the great support from others I would not have been able to finish this thesis. Especially I want to thank . . .

- Prof. Keimer for hosting me as a PhD student in his department and continuous support throughout the thesis
- Prof. Michler for co-examining this thesis
- Prof. Büchler for acting as the examination chairperson
- Prof. v. Klitzing for giving me the opportunity to work in his department and his catchy enthusiasm regarding the quantum Hall effect
- Jurgen Smet for equipping me with hints, instruments, helpful advises to this thesis and the freedom to follow different routes
- Hans G. Libuda for supporting the Max-Planck research school
- Ivan Dmitriev for various explanations regarding MIRO
- Joseph Falson and the Kawasaki group for outstanding oxide samples
- Igor Kukushkin and his team for the scientific exchange and discussions
- Sergey Dorozhkin for joint science at the He3 system
- Steffen Wahl and Gunther Euchner for great technical support
- Achim Gueth, Marion Hagel, Ulrike Waizmann, Sanela Goeres, Thomas Reindl and Jurgen Weis for great support in the cleanroom
- Ruth Jenz for her sincere help in all administrative cases
- Matthias Kühne, Benedikt Frieß, Federico Paolucci, Marcel Mausser, Ding Zhang, Benjamin Krauss, Johannes Nübler and Thomas Beringer for scientific and especially non-scientific advises
- all the other colleagues for a cooperative and pleasant working atmosphere
- my wonderful wife and family for backing me up

